

# A public relativistic transfer function model for X-ray reverberation mapping of accreting black holes

Adam Ingram<sup>1</sup>\*, Guglielmo Mastroserio<sup>2</sup>, Thomas Dauser<sup>3</sup>, Pieter Hovenkamp<sup>2</sup>, Michiel van der Klis<sup>2</sup> & Javier A. García<sup>4,3</sup>

<sup>1</sup>Department of Physics, Astrophysics, University of Oxford, Denys Wilkinson Building, Keble Road, Oxford, OX1 3RH, UK

<sup>2</sup>Anton Pannekoek Institute, University of Amsterdam, Science Park 904, 1098 XH Amsterdam, The Netherlands

<sup>3</sup>Remeis Observatory & ECAP, Universität Erlangen-Nürnberg, D-96049 Bamberg, Germany

<sup>4</sup>Cahill Center for Astronomy and Astrophysics, California Institute of Technology, Pasadena, CA 91125, USA

Accepted 2019 June 18. Received 2019 June 15; in original form 2019 April 26

## ABSTRACT

We present the publicly available model RELTRANS that calculates the light-crossing delays and energy shifts experienced by X-ray photons originally emitted close to the black hole when they reflect from the accretion disk and are scattered into our line-of-sight, accounting for all general relativistic effects. Our model is fast and flexible enough to be simultaneously fit to the observed energy-dependent cross-spectrum for a large range of Fourier frequencies, as well as to the time-averaged spectrum. This not only enables better geometric constraints than only modelling the relativistically broadened reflection features in the time-averaged spectrum, but additionally enables constraints on the mass of supermassive black holes in active galactic nuclei and stellar-mass black holes in X-ray binaries. We include a self-consistently calculated radial profile of the disk ionization parameter and properly account for the effect that the telescope response has on the predicted time lags. We find that a number of previous spectral analyses have measured artificially low source heights due to not accounting for the former effect and that timing analyses have been affected by the latter. In particular, the magnitude of the soft lags in active galactic nuclei may have been under-estimated, and the magnitude of lags attributed to thermal reverberation in X-ray binaries may have been over-estimated. We fit RELTRANS to the lag-energy spectrum of the Seyfert galaxy Mrk 335, resulting in a best fitting black hole mass that is smaller than previous optical reverberation measurements ( $\sim 7$  million compared with  $\sim 14 - 26$  million  $M_\odot$ ).

**Key words:** black hole physics – methods: data analysis – galaxies: active – X-rays: binaries.

## 1 INTRODUCTION

Stellar-mass black holes in X-ray binary systems and supermassive black holes in active galactic nuclei (AGN) are thought to accrete via a geometrically thin, optically thick accretion disk, which radiates thermally (Shakura & Sunyaev 1973; Novikov & Thorne 1973). The hard X-ray spectrum is often dominated by a power-law component with a high energy cut off, thought to be due to Compton up-scattering of comparatively cool photons in a cloud (with optical depth  $\tau \sim 1 - 2$ ) of hot electrons located close to the black hole (Thorne & Price 1975; Sunyaev & Truemper 1979). The exact geometry of this cloud is still debated, with

suggested models including a standing shock at the base of the jet (Miyamoto & Kitamoto 1991; Fender et al. 1999), a coronal layer sandwiching the disk (Galeev et al. 1979; Haardt & Maraschi 1991), and evaporation of the inner disk regions to form a hot, large scale height accretion flow (*the truncated disk model*; Eardley et al. 1975; Ichimaru 1977; Done et al. 2007). In the absence of a consensus on its geometry, the Comptonising region is often simply referred to as the corona, a convention that we will employ here.

We observe Comptonized radiation that reaches us directly from the corona (the *direct* component) in addition to coronal emission that has been reprocessed and re-emitted in the upper atmosphere of the disk, conventionally called the *reflection* component. These ‘reflected’ photons imprint characteristic features onto the observed spectrum including a prominent iron K $\alpha$  emission line at  $\sim 6.4$  keV and

\* E-mail: adam.ingram@physics.ox.ac.uk

a so-called reflection hump peaking at  $\sim 20 - 30$  keV (e.g. Lightman & Rybicki 1980; George & Fabian 1991; Ross & Fabian 1993; García & Kallman 2010). The iron line provides a powerful probe of the disk dynamics and geometry, since its shape is observed to be distorted by photon energy shifts caused by relativistic orbital motion of disk material and gravitational redshift (Fabian et al. 1989; Laor 1991). If the disk inner radius inferred from the line profile is sufficiently small, setting it equal to the innermost stable circular orbit (ISCO) of general relativity (GR) provides an estimate for the spin of the black hole.

Many studies have used reflection spectroscopy to probe both AGN (e.g. Tanaka et al. 1995; Reynolds & Nowak 2003; Patrick et al. 2012; Walton et al. 2013; Risaliti et al. 2013) and black hole X-ray binary (e.g. Miller 2007; Reis et al. 2009; Miller et al. 2013; Kolehmainen et al. 2014; Plant et al. 2014; García et al. 2015) accretion flows. This has yielded many measurements of high black hole spin in AGN (e.g. Reynolds 2019; Middleton 2016), although complex line-of-sight absorption can potentially introduce modelling systematics (e.g. Miller et al. 2008). For the binaries, spectral modelling studies often conclude that the inner radius moves towards the black hole as the spectrum evolves from the hard power-law dominated *hard state* to the thermal disk dominated *soft state* on timescales of  $\sim$ months (Done et al. 2007; Plant et al. 2014; García et al. 2015). However, even though there is broad agreement in the *trend* in disk inner radius, the measured *values* themselves vary enormously between different studies (García et al. 2015), with potential systematics including calibration uncertainty (e.g. Done & Diaz Trigo 2010) and the difficulty of disentangling the direct and reflected components (e.g. Basak et al. 2017).

The degeneracies associated with spectral modelling can be addressed by additionally modelling the light-crossing delay between variations in the direct and reflected spectral components (Campana & Stella 1995; Reynolds et al. 1999; Uttley et al. 2014). Such reverberation mapping techniques therefore promise better constraints on the disk geometry (and therefore the black hole spin), but also entirely new constraints on black hole mass (Stella 1990). This is essentially because the delays depend on physical distances, whereas the energy shifts are only sensitive to distances in units of gravitational radii ( $R_g = GM/c^2$ ). Fourier frequency dependent time lags between energy channels can be calculated from the argument of the cross-spectrum (van der Klis et al. 1987). It is routinely found that, at low Fourier frequencies ( $\nu \lesssim 1.5 \times 10^{-3} c/R_g$ ), hard photons lag soft, both for the binaries (Miyamoto et al. 1988; Nowak et al. 1999; Kotov et al. 2001) and AGN (e.g. Papadakis et al. 2001; McHardy et al. 2004; Epitropakis & Papadakis 2017). These *intrinsic hard lags* are thought to be caused by spectral variability of the direct component rather than reverberation, due to their large magnitude and the lack of reflection features in their energy dependence, and may originate from inward propagation of fluctuations in the mass accretion rate (Arévalo & Uttley 2006; Ingram & van der Klis 2013; Rapisarda et al. 2017b; Mahmoud & Done 2018). Since the hard lags reduce with frequency, it has been possible to detect reverberation signatures at high frequencies in AGN, first through soft lags interpreted as the soft-excess of the reflection spectrum lagging the direct radiation (Fabian et al. 2009; De Marco et al. 2013), and later through an iron line feature in the lag-

energy spectrum (Zoghbi et al. 2012; Kara et al. 2016). A number of studies have focused on modelling these high frequency lags in AGN (Cackett et al. 2014; Emmanoulopoulos et al. 2014; Epitropakis et al. 2016; Chainakun et al. 2016; Wilkins et al. 2016; Caballero-Garcia et al. 2018). Discoveries of reverberation signals came a little later for the binaries, since the cross over from intrinsic to reverberation lags is at a much higher frequency (measured in Hz rather than  $c/R_g$ ) for a stellar-mass black hole (due to mass scaling), and therefore the signal is harder to pick out of the Poisson noise. Still, soft lags, interpreted as reverberation of thermally re-processed photons, have been detected (Uttley et al. 2011; De Marco et al. 2015 - although this could feasibly result from backwards propagation of accretion rate fluctuations: Mushtukov et al. 2018), and iron K lags were finally detected for MAXI J1820+070 by Kara et al. (2019) using the *Neutron star Interior Composition Explorer* (NICER; Gendreau et al. 2016).

Still further information is contained in the energy and frequency dependent variability amplitude, which can also be measured from the cross-spectrum. This can provide powerful constraints, since the variability amplitude of reflected emission should be washed out at the highest frequencies due to destructive interference between rays reflected from different parts of the disk (Gilfanov et al. 2000). It is optimal to consider all of these properties simultaneously<sup>1</sup>. The neatest way to do this statistically is to jointly model the time-averaged spectrum and the real and imaginary parts of the energy dependent cross-spectrum (Mastroserio et al. 2018). Here we present a public XSPEC model that enables such an analysis. We define two versions of the model, RELTRANS and RELTRANS<sub>CP</sub>, which represent the direct spectral component respectively as an exponentially cut-off power-law and using the model NTHCOMP. We assume a simple lamppost geometry (Matt et al. 1991; Martocchia & Matt 1996), which allows all GR effects to be properly accounted for without prohibitive computational expense - although we note that it is simple in our formalism to consider a number of lamppost sources. Source code and usage instructions can be downloaded from <https://adingram.bitbucket.io/>.

We present a detailed derivation of our model in Section 2 and explore its properties in Section 3. Our treatment properly accounts for line-of-sight absorption and the telescope response, and the model accounts for the radial dependence of the disk ionization parameter. In Section 4 we investigate the importance of these effects. In Section 5, we perform a proof-of-principle fit to the lag-energy spectrum of the narrow-line Seyfert 1 galaxy Mrk 335 for a single frequency range. We discuss and conclude our findings in Sections 6 and 7.

## 2 DERIVATION OF THE CROSS-SPECTRUM IN THE LAMPPOST GEOMETRY

Here we derive the time-dependent observed energy spectrum assuming an isotropically radiating lamppost source located on the black hole spin axis a height  $h$  above the

<sup>1</sup> Indeed, also considering the power spectrum additionally provides information on the coherence between energy bands (e.g. Rapisarda et al. 2016), which we ignore here.

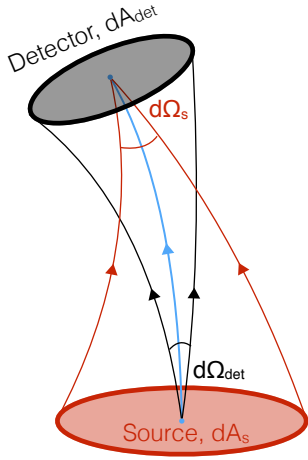


**Figure 1.** Schematic of a source and detector with surface areas (measured in their own restframes)  $dA_s$  and  $dA_{det}$  respectively. The blue line represents a photon path that emerges parallel to the source surface area vector (in the source restframe) and arrives parallel to the detector surface area vector (in the detector restframe). Only photons emerging from the source within the solid angle  $d\Omega_{det}$  will eventually hit the detector. The solid angles and surface areas are related through the reciprocity theorem (equation 2).

hole, and use the Fourier transform to calculate the energy dependent cross-spectrum as a function of Fourier frequency  $\nu$ . We assume that the specific (energy) flux (i.e. energy per unit time per unit area per unit photon energy) seen by a distant observer as a function of photon energy,  $E$ , and time  $t$ , both defined in the observer's restframe, is given by

$$S(E, t) = F(E, t) + R(E, t). \quad (1)$$

The first and second terms on the right hand side represent respectively the direct and reflected spectral components. In this paper, we ignore directly observed disk radiation, assuming it to be below our X-ray bandpass. This is appropriate for AGN, and hard state X-ray binaries in the  $E \gtrsim 3$  keV bandpass.

In this section, we first go over some general considerations of radiation theory in GR (Section 2.1). We then derive the observed time-dependent direct spectrum (Section 2.2) and the reflection spectrum (Section 2.3), before deriving the transfer function that we will use for our reverberation model (Section 2.4), followed by the kernel used to calculate our transfer function (Section 2.5). Finally we will discuss the so-called reflection fraction (Section 2.6).

## 2.1 Reciprocity and Liouville's theorem

Fig 1 shows a schematic of a source with surface area  $dA_s$  in its own rest frame and a detector with surface area  $dA_{det}$  in its own rest frame. Photons travel along null geodesics, which are solutions to the geodesic equation with line element  $ds^2 = g_{\mu\nu}dx^\mu dx^\nu = 0$ . Here,  $g_{\mu\nu}$  is the metric and  $dx^\mu$  is the coordinate interval corresponding to an interval  $ds/c$  in proper time. Throughout this paper, we use the Kerr metric in Boyer-Lindquist coordinates. The position of a photon along its geodesic is described by the affine pa-

rameter  $\lambda$  and its trajectory described by the tangent vector  $k^\mu(\lambda) = dx^\mu/d\lambda$ . The blue line in Fig 1 represents the unique null-geodesic,  $k^\mu(\lambda)$ , that connects the centre of the source to the centre of the detector. For this example, the geodesic begins parallel to the source's surface area vector and ends parallel to the detector's surface area vector, but we can generalize by specifying  $dA_{det}$  and  $dA_s$  to be respectively the *projected* area of the detector and source perpendicular to  $k^\mu$  in the local restframe. The black lines depict the trajectory of photons that emerge from the centre of the source and hit the edge of the detector, representing a bundle of photons that diverge from the centre of the source around  $k^\mu(\lambda)$ , subtending a solid angle  $d\Omega_{det}$  in the source rest frame (i.e. all the photons in the bundle hit the detector and all others miss). The red lines depict the trajectory of photons that emerge from the edge of the source and hit the centre of the detector, representing a bundle of geodesics that converge onto the centre of the detector around  $k^\mu(\lambda)$ , subtending a solid angle  $d\Omega_s$  in the detector rest frame. This is the solid angle that the source subtends on the detector's sky (i.e. all photons from the bundle hit the centre of the detector and all others miss the centre).

These four quantities are related by the general relativistic reciprocity theorem

$$g_{so}^2 dA_{det} d\Omega_s = dA_s d\Omega_{det}. \quad (2)$$

Here  $g_{so} = E_o/E_s$  is the blueshift<sup>2</sup> experienced by photons traveling from source to detector and  $E_o$  and  $E_s$  are respectively the energy of the photon as measured in the rest frame of the detector and source (see Appendix B for expressions of blueshift factors in the Kerr metric). The reciprocity theorem in GR was first derived by Etherington (1933), and a more concise presentation of the derivation can be found on pages 631-633 of Ellis (2009, this is a republication of the original 1971 proceeding). Ellis (2007) provides a useful commentary on the original Etherington paper. This is an intriguing geometrical result, showing that the curvature of spacetime does not influence the relationship between these solid angles and surface areas: the reciprocity theorem in GR is the same as that in special relativity for a given blueshift factor. We can even recover the classical reciprocity theorem by transforming  $d\Omega_{det}$  into the detector frame to cancel out the  $g_{so}^2$ . The blueshift is calculated as

$$g_{so} = \frac{(k_{det})^\mu (u_{det})_\mu}{(k_s)^\nu (u_s)_\nu}, \quad (3)$$

where  $u_s$  and  $u_{det}$  are respectively the 4-velocity of the source and detector.

If  $dN(E_s)$  photons with energies ranging from  $E_s$  to  $E_s + dE_s$  are radiated isotropically from the flat source surface in its restframe, a fraction  $d\Omega_{det}/\pi$  of them will cross the detector some time later<sup>3</sup>. Their energies will be measured to range from  $E_o$  to  $E_o + dE_o$  in the detector rest frame, meaning that the number of photons crossing the detector is

<sup>2</sup> i.e.  $g_{so} > 1$  corresponds to a blueshift and  $g_{so} < 1$  to a redshift. Note that  $g_{so} = 1/(1 + z_{so})$ , where  $z_{so}$  is redshift defined in the traditional sense of fractional change in wavelength.

<sup>3</sup> This is because the projected area of the source is  $\propto \cos \theta$  if it is viewed from inclination  $\theta$  (and  $d\Omega = d\cos \theta d\phi$ ). Therefore the fraction is  $d\Omega / \int_0^{2\pi} \int_0^1 \cos \theta d\cos \theta d\phi = d\Omega / \pi$

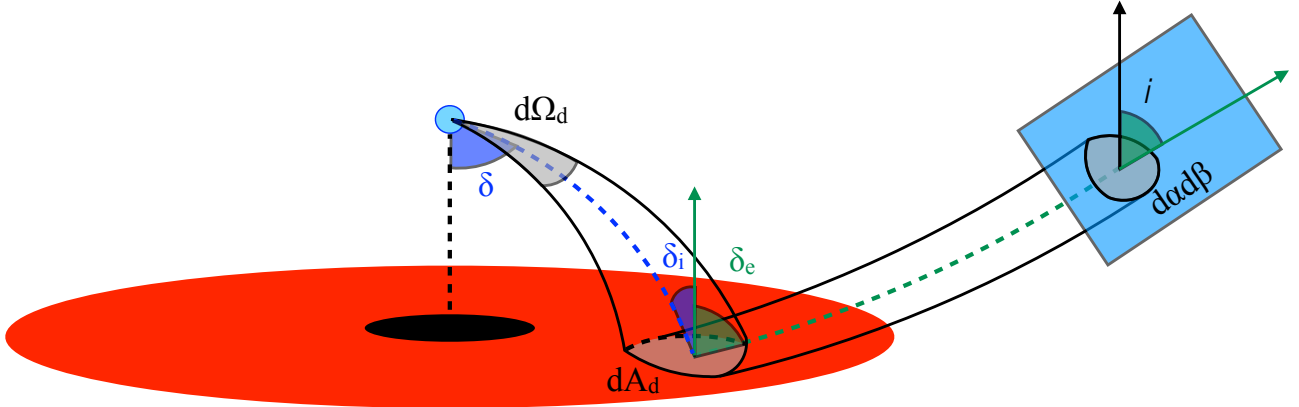


**Figure 2.** Schematic of the on-axis lamppost geometry. A disk patch with area  $dA_d$  subtends a solid angle  $d\Omega_d$  according to the irradiating source. The disk patch corresponds to an area  $d\alpha d\beta$  on the image plane, where  $\alpha$  and  $\beta$  are respectively horizontal and vertical impact parameters at infinity. The bundle of rays within the represented solid angle are assumed to follow the trajectory (green dashed lines) defined by the initial ( $\delta$ ), incidence ( $\delta_i$ ), emission ( $\delta_e$ ) and inclination ( $i$ ) angles.

$dN_o(E_o) = dN(E_s)d\Omega_{det}/\pi$ . The specific (energy) flux crossing the detector is therefore

$$\begin{aligned} F_o(E_o, t_o) &\equiv \frac{E_o dN_o(E_o)}{dt_o dE_o dA_{det}} \\ &= \frac{g_{so}}{\pi} \frac{E_s dN(E_s)}{dt_s dE_s dA_s} dA_s \frac{d\Omega_{det}}{dA_{det}} \\ &= \frac{g_{so}}{\pi} F_s(E_s) dA_s \frac{d\Omega_{det}}{dA_{det}}, \end{aligned} \quad (4)$$

where  $F_s(E_s)$  is the specific flux radiated by the source,  $dt_s = g_{so} dt_o$  and we have used  $dE_o/dE_s = g_{so}$ . Rearranging the above equation and applying the reciprocity theorem (equation 2) gives the rather familiar formula

$$I_o(E_o) = g_{so}^3 I_s(E_s), \quad (5)$$

where  $I_o(E_o)$  and  $I_s(E_s)$  are specific intensities: specific flux per unit solid angle (in this case  $I_o(E_o) = F_o(E_o)/d\Omega_s$  and  $I_s(E_s) = F_s(E_s)/\pi$ ). This famous result can also be derived from Liouville's theorem, which states that the number of photons per unit volume in phase space is Lorentz invariant (see e.g. Lindquist 1966; Misner et al. 1973). The derivation presented here is perhaps more intuitive. Integrating both sides over all observed energies gives the familiar expression for bolometric flux in terms of bolometric intensity

$$F_o = g_{so}^4 I_s d\Omega_s. \quad (6)$$

We can understand intuitively where these four factors of blue shift originate. Two come from the adjustment to solid angle in the reciprocity theorem (equation 2 - and these two factors can further be understood as special relativistic aberration in the small angle limit), one comes from the adjustment to the energy of each photon and one comes from the adjustment to time intervals (i.e. bolometric flux is  $\propto E dN/dt$ ). Finally, all blue shifts in this paper are calculated in the Kerr metric, which is asymptotically flat and stationary and therefore does not account for cosmological redshift. An observer at cosmological redshift  $z$  will therefore measure a specific intensity

$$I(E) = \left( \frac{g_{so}}{1+z} \right)^3 I_s(E_s), \quad (7)$$

and will measure time intervals  $\tau = (1+z)\tau_o$  (cosmological time dilation).

## 2.2 Direct spectrum

We assume a spherical X-ray source, with surface area in its own rest frame  $a_s$ , that isotropically radiates a specific flux

$$F_s(E_s, t'_o) = \frac{C(t'_o)}{a_s} f(E_s | \Gamma, E_{cut}), \quad (8)$$

where  $t'_o$  is time in the restframe of an observer at cosmological redshift  $z = 0$ . In the RELTRANS version of the model, the direct spectrum is

$$f(E | \Gamma, E_{cut}) \propto E^{1-\Gamma} e^{-E/E_{cut}}, \quad (9)$$

where the constant of proportionality will be calculated below. The RELTRANS version instead uses the thermal Comptonisation model NTHCOMP (Zdziarski et al. 1996; Życki et al. 1999), with the  $E_{cut}$  parameter replaced by the electron temperature  $kT_e$ . For the purposes of this derivation, we will always use  $E_{cut}$ , on the understanding that this can be replaced with  $kT_e$  for the case of the NTHCOMP version. In order to evaluate the function  $f(E)$  in these two cases, we use the model XILLVER and XILLVERCP respectively (García & Kallman 2010; García et al. 2013), which we will also use in order to calculate the restframe reflection spectrum. Our code calls the relevant XILLVER model with the reflection fraction parameter set to zero, which returns the illuminating spectrum used for the calculation of the reflection spectrum.

In this paper, as can be seen in Equation (8), we will only consider *linear* variability of the source flux. That is, the shape of the direct component of the spectrum remains constant in time and only the normalisation varies. In future versions, we will extend our modelling to account for non-linear variations of the spectrum radiated by the corona using the Taylor expansion technique described in Mastroserio et al. (2018).

We assume the source is small enough to ensure that any light rays that pass by either side of it on route to the distant observer are parallel to one another (i.e. spacetime

is approximately flat on the scale of the source area). The projected area of the source is therefore  $dA_s = a_s/4$ . Substituting this into equation 4 gives the observed specific flux at time  $t_o$

$$\begin{aligned} F_o(E_o, t_o) &= \frac{g_{so}}{4\pi} F_s(E_s, t'_o) a_s \frac{d\Omega_{det}}{dA_{det}} \\ &= \frac{C(t'_o)}{4\pi} g_{so} f(E_o|\Gamma, g_{so} E_{cut}) \frac{d\Omega_{det}}{dA_{det}}, \end{aligned} \quad (10)$$

where  $t_o = t'_o + \tau_{so}$  and  $\tau_{so}$  is the time it takes photons to travel from source to detector, as measured in the detector frame (and assuming  $z = 0$ ). The second line of the above equation is exact for an exponentially cut-off power-law illuminating spectrum but only approximate for an NTHCOMP spectrum. The final term on the right hand side accounts for lensing / de-lensing due to light bending. Defining the inclination angle  $i$  as the angle between the black hole spin axis and the trajectory of photons when they cross the detector (see Fig 2, but note that photons reach the detector both directly and via reflection) and  $D = \sqrt{dA_s/d\Omega_s}$  as the distance between the source and the detector (and also, to a very good approximation, the distance between the hole and the detector, since  $D \gg h$ ), the detector area is  $dA_{det} = D^2 \sin i \, di \, d\phi$ . Defining  $\delta$  as the angle, measured in the source rest frame, between the spin axis and the emergent trajectory of a photon as it is radiated by the source (see Fig 2 for an example of a photon that reflects from the disk, but note that photons with larger  $\delta$  may reach the observer directly), we can write

$$\frac{d\Omega_{det}}{dA_{det}} = \frac{1}{D^2} \left| \frac{d \cos \delta}{d \cos i} \right| = \frac{\ell}{D^2}, \quad (11)$$

since intervals in azimuth  $d\phi$  are constant along a geodesic for an on-axis source in the Kerr metric. We calculate the lensing factor,  $\ell = |d \cos \delta / d \cos i|$ , numerically by tracing rays along null geodesics in the Kerr metric, calculated using the publicly available code YNOGK (Yang & Wang 2013), which is based on another publicly available code GEOKERR (Dexter & Agol 2009). The observed specific flux is therefore

$$F_o(E_o, t_o) = A(t'_o) \ell g_{so}^\Gamma f(E_o|\Gamma, g_{so} E_{cut}), \quad (12)$$

where we have defined  $A(t) \equiv C(t)/(4\pi D^2)$ . An observer at a cosmological distance sees a specific flux

$$F(E, t) = A(t') \ell \left( \frac{g_{so}}{1+z} \right)^\Gamma f[E|\Gamma, g_{so} E_{cut}/(1+z)], \quad (13)$$

and measures a time interval  $t - t' = (1+z)\tau_{so}$ . In our model, for consistency with the RELXILL family of models (Dauser et al. 2013; García et al. 2014), we specify as a model parameter the cut-off energy in the *observer's* frame,  $(E_{cut})_{obs} = g_{so} E_{cut}/(1+z)$ . When the verbose level is set suitably high, the code prints to screen the value of the cut-off energy in the source restframe. For RELTRANSCP, we instead specify the parameter  $(kT_e)_{obs} = g_{so} kT_e/(1+z)$ .

### 2.3 Reflection spectrum

Fig. 2 illustrates the source irradiating a patch of the disk that subtends a solid angle  $d\Omega_d$  in the *source* rest frame and has a surface area  $dA_d$  in the reference frame of the *disk patch*. Again using equation 4, the specific flux crossing the

surface of the disk patch, in the restframe of the disk patch is

$$F_{d,in}(E_d, t'_o) = \frac{C(t'_o - \tau_{sd})}{4\pi} g_{sd}^\Gamma f(E_d|\Gamma, g_{sd} E_{cut}) \frac{d\Omega_d}{dA_d}. \quad (14)$$

The irradiating flux is all re-processed into the reflection spectrum, which is radiated an-isotropically from the disk upper surface ( $\mu_e = \cos \delta_e \geq 0$ ; see Fig. 2). The emission angle-dependent reflected specific intensity  $I_{d,out}$  emergent from the disk is related to the incident flux  $F_{d,in}$  as

$$\int_0^\infty F_{d,in}(E_d, t'_o) dE_d = 2\pi \int_0^1 \int_0^\infty I_{d,out}(E_d, t'_o|\mu_e) \mu_e dE_d d\mu_e. \quad (15)$$

As alluded to in the previous section, we use XILLVER or XILLVERCP to calculate the reflected specific intensity  $\mathcal{R}(E|\mu_e)$  for an illuminating specific flux  $f(E|\Gamma, E_{cut})$  (we set the reflection fraction parameter to  $-1$ , where the minus sign ensures that the XILLVER model returns only the reflection spectrum rather than summing it with the incident spectrum). The XILLVER models are normalized such that

$$\begin{aligned} \frac{1}{2} \int_0^1 \int_0^\infty \mu_e \mathcal{R}(E|\mu_e, \Gamma, E_{cut}, \log_{10} \xi) dE d\mu_e \\ = \int_0^\infty f(E|\Gamma, E_{cut}, \log_{10} \xi) dE, \end{aligned} \quad (16)$$

where  $\xi(r) = 4\pi F_x(r)/n_e(r)$  is the ionization parameter,  $F_x(r)$  is the 13.6 eV to 13.6 keV illuminating flux and  $n_e(r)$  is the electron number density.

Inspection of equations (14), (15) and (16) shows

$$I_{d,out}(E_d, t'_o|\mu_e) = \frac{1}{2} \frac{C(t'_o - \tau_{sd})}{2\pi} g_{sd}^\Gamma \frac{d\Omega_d}{dA_d} \frac{\mathcal{R}(E_d|\mu_e, g_{sd} E_{cut})}{4\pi}. \quad (17)$$

Once more exploiting the symmetry of the lampost geometry, we can consider the case whereby the disk patch is an annulus at  $r$  with width  $dr$  to find

$$\frac{d\Omega_d}{dA_d} = 2\pi \frac{|d \cos \delta/dr|}{dA_{ring}/dr}. \quad (18)$$

It is important to note that the angle  $\delta$  in the equation is defined in the source restframe, whereas the area  $dA_{ring}$  is defined in the restframe of the disk annulus. The radial coordinate is defined in Boyer-Lindquist coordinates. We calculate  $d \cos \delta/dr$  and  $\tau_{sd}$  numerically using YNOGK. We calculate the area differential analytically. In Boyer-Lindquist coordinates, the area of a disk annulus with radial extent  $dr$  is  $d^2x = 2\pi\sqrt{g_{\phi\phi}g_{rr}}dr$ . The area in the rest frame of the rotating annulus is  $dA_{ring} = \gamma^\phi d^2x$ , where  $\gamma^\phi$  is the Lorentz factor of the annulus (e.g. Wilkins & Fabian 2012). We present a derivation for  $\gamma^\phi$  in Appendix A, pointing out some very small (largely inconsequential) errors in previous derivations (Bardeen et al. 1972; Dauser et al. 2013).

According to the stationary observer, the disk patch centered at disk coordinates  $r, \phi$  is centered on coordinates on the observer plane  $\alpha, \beta$  and subtends a solid angle  $d\Omega = d\alpha d\beta / D^2$  (see Fig 2). Here  $\alpha$  and  $\beta$  are the impact parameters at infinity. The specific flux seen from the disk patch with coordinates  $r, \phi$  by the stationary observer viewing from an inclination angle  $i$  (with  $\mu = \cos i$ ) is therefore

$$dR_o(E_o, t_o) = g_{do}^3 I_{d,out}(E_o/g_{do}, t_o - \tau) d\alpha d\beta / D^2, \text{ giving}$$

$$dR_o(E_o, t_o | \mu, r, \phi) = A[t_o - \tau(r, \phi)] g_{do}^3(r, \phi) \epsilon(r)$$

$$\times \mathcal{R}[E_o/g_{do}(r, \phi) | \mu_e(r, \phi), g_{sd}(r) E_{cut}, \log_{10} \xi(r)] d\alpha d\beta, \quad (19)$$

where

$$\epsilon(r) = \frac{g_{sd}^{\Gamma}(r)}{2} \frac{|d \cos \delta / dr|}{dA_{\text{ring}} / dr} \quad (20)$$

is the radial emissivity profile and  $\tau(r, \phi) = \tau_{sd}(r) + \tau_{do}(r, \phi) - \tau_{so}$ . Note that for equation 19 we have used equation (5), since  $d\alpha d\beta / D^2$  is the solid angle subtended by the disk patch according to the observer in the observer's restframe. Also note that the cosine of the emission angle,  $\mu_e$ , is a function of  $r$  and  $\phi$  because bending of rays leads to photons with the same final trajectory having different initial trajectories (García et al. 2014). The total reflection spectrum seen by the stationary observer is then calculated by integrating equation (19) over all impact parameter values for which the corresponding geodesic intercepts the disk at radii  $r_{in} < r < r_{out}$ .

## 2.4 Transfer function and cross-spectrum

We can express the total reflected specific flux seen by the  $z = 0$  observer as  $R_o(E_o, t_o) = A(t_o) \otimes w_o(E_o, t_o)$ , where  $\otimes$  denotes a convolution and

$$w_o(E_o, t_o) = \int_{\alpha} \int_{\beta} \epsilon(r) g_{do}^3(r, \phi) \delta(t_o - \tau(r, \phi))$$

$$\times \mathcal{R}[E_o/g_{do}(r, \phi) | \mu_e(r, \phi), g_{sd}(r) E_{cut}, \log_{10} \xi(r)] d\alpha d\beta. \quad (21)$$

is the *impulse-response function*. In Fourier space the convolution is a multiplication, so it is best to Fourier transform the impulse response function to get the *transfer function*

$$W_o(E_o, \nu) = \int_{\alpha} \int_{\beta} \epsilon(r) g_{do}^3(r, \phi) e^{i2\pi\tau(r, \phi)\nu}$$

$$\times \mathcal{R}[E_o/g_{do}(r, \phi) | \mu_e(r, \phi), g_{sd}(r) E_{cut}, \log_{10} \xi(r)] d\alpha d\beta. \quad (22)$$

Setting  $\nu = 0$  (The DC component, standing for direct current), gives the time-averaged spectrum. Generalising to an observer at a cosmological distance gives  $R(E, \nu) = A(\nu)W(E, \nu)$ , where

$$W(E, \nu) = (1+z)^{-3} \int_{\alpha} \int_{\beta} \epsilon(r) g_{do}^3(r, \phi) e^{i2\pi(1+z)\tau(r, \phi)\nu}$$

$$\times \mathcal{R}[E_o/g_{do}(r, \phi) | \mu_e(r, \phi), g_{sd}(r) E_{cut}, \log_{10} \xi(r)] d\alpha d\beta, \quad (23)$$

and we note that  $A(\nu)$  is in general complex. We trace rays defined by given impact parameter values backwards from the observer plane towards the black hole along the relevant null geodesic in the Kerr metric (again calculated using YNOGK). This operation automatically accounts for lensing of rays travelling from the disk to the observer. We consider a  $400 \times 400$  grid of impact parameters with  $\sqrt{\alpha^2 + \beta^2} \leq 300 R_g$ . We additionally consider a larger grid with  $300 R_g < \sqrt{\alpha^2 + \beta^2} \leq r_{out}$  for which we calculate geodesics in the Minkowski metric. For rays that cross the disk mid-plane, we calculate the  $r$ ,  $\phi$  and  $t$  coordinates at the crossing point. We stop following rays after the first time they cross the mid-plane, therefore ignoring ghost images, which are likely blocked in reality by material in the vicinity of the hole. We quote the formulae for the blueshift factors and angles in Appendix B. We also include a 'boosting

factor' to account for the likelihood that our assumption of an isotropically radiating source is inappropriate. We specify the factor  $1/\mathcal{B}$  as a model parameter, such that  $1/\mathcal{B} < 1$  roughly corresponds to the source being beamed towards us and away from the disk.

From the transfer function, we can calculate the energy-dependent cross-spectrum. This is a series of cross-spectra between the flux at each energy and that in a common reference band,  $G(E, \nu) = S(E, \nu)F_r^*(\nu)$ . In our model, this is given by

$$G(E, \nu) = \alpha(\nu) e^{i\phi_A(\nu)} \left[ F_{A=1}(E) + \frac{W(E, \nu)}{\mathcal{B}} \right], \quad (24)$$

where  $\alpha(\nu)$  and  $\phi_A(\nu)$  are model parameters for each frequency  $\nu$ , and  $F_{A=1}(E)$  is given by equation (13) with  $A = 1$ . We could equally see equation 24 as a formula for the *complex-covariance* (Mastroserio et al. 2018), which is simply the cross-spectrum divided through by the amplitude of the reference band,  $S(E, \nu)F_r(\nu)/|F_r(\nu)|$ . The only adjustment would be a slight change in the, already fairly arbitrary, meaning of the normalisation parameter  $\alpha(\nu)$ . Finally, line-of-sight absorption is accounted for using the multiplicative XSPEC model, TBABS (Wilms et al. 2000), such that the transmitted cross-spectrum is  $G_{abs}(E, \nu) = \text{TBABS}(E) \times G(E, \nu)$ . For a given frequency range, our model calculates this transmitted cross-spectrum and outputs, as a function of energy, the real part of this, the imaginary part, the modulus (energy-dependent variability amplitude) or the time lag ( $t_{\text{lag}}(E, \nu) = \arg\{G(E, \nu)\}/[2\pi\nu]$ ), depending on the user-defined mode.

As discussed in Mastroserio et al. (2018), if the reference band is the sum of energy channels ranging from  $I_{min}$  to  $I_{max}$  that are all well calibrated for the instrument we are observing with, the parameter  $\phi_A(\nu)$  need not be a free parameter, and can instead be expressed as

$$\tan \phi_A(\nu) = \frac{-\sum_{J=I_{min}}^{I_{max}} \Im[W(J, \nu)]/\mathcal{B}}{\sum_{I=I_{min}}^{I_{max}} F_{A=1}(I) + \Re[W(I, \nu)]/\mathcal{B}}. \quad (25)$$

Here,  $F_{A=1}(I)$  and  $W(I, \nu)$  are calculated by convolving  $\text{TBABS}(E) \times F_{A=1}(E)$  and  $\text{TBABS}(E) \times W(E, \nu)$  respectively with the instrument response (see Mastroserio et al. 2018 for details). Our model incorporates both a mode in which  $\phi_A(\nu)$  is a free parameter and a mode in which the instrument response is read in and  $\phi_A(\nu)$  is calculated self-consistently.

## 2.5 The reflection kernel

Much of the computational expense of evaluating equation (22) can be saved by representing it as a convolution with a kernel. The easiest case to calculate is if we assume that the shape of the rest frame reflection spectrum depends on neither  $r$  nor  $\phi$ . This can be done by assuming that the cut-off energy seen by each disk patch is  $E_{cut}$  rather than  $g_{sd}(r)E_{cut}$ , that  $\delta_e(r, \phi) = i$  and that the disk ionization parameter is independent of radius. Working with  $\log E$  rather than  $E$ , allows the transfer function to be represented as

$$W(\log E, \nu) = \int_0^{\infty} \mathcal{R}(\log E') W_{\delta}(\log(E/E'), \nu) d\log E', \quad (26)$$

where

$$W_\delta(\log E, \nu) = (1+z)^{-3} \int_{\alpha, \beta} \epsilon(r) g_{do}^3(r, \phi) e^{i2\pi(1+z)\tau(r, \phi)\nu} \times \delta \left[ \log E - \log \left( \frac{g_{do}(r, \phi)}{1+z} \right) \right] dr d\phi \quad (27)$$

is the kernel of the transfer function. It is clear that the kernel is simply the transfer function for a  $\delta$ -function rest frame reflection spectrum centered at 1 keV. Equation (26) can be recognised as a convolution in  $\log E$  space, and can thus be written

$$W(\log E, \nu) = \mathcal{R}(\log E) \otimes_{\log E} W_\delta(\log E, \nu). \quad (28)$$

We compute the convolution using the convolution theorem (i.e. Fourier transforming both, multiplying and finally inverse transforming), which allows us to exploit the large gain in speed afforded by using the fast Fourier transform (FFT) algorithm.

In the more general case, we can quantise  $\mu_e$ ,  $g_{sd}$  and  $\log_{10} \xi$  by defining a number of discrete bins for each and writing the transfer function as

$$W(\log E, \nu) = \sum_j \sum_k \sum_n \mathcal{R}[\log E | \mu_e(j), g_{sd}(k), \log_{10} \xi(n)] \otimes_{\log E} W_\delta(\log E, \nu | j, k, n), \quad (29)$$

where  $W_\delta(\log E, \nu | j, k, n)$  is given by equation 27, except the integrand is only non-zero for disk patches with  $\mu_e(r, \phi)$ ,  $g_{sd}(r)$  and  $\log_{10} \xi(r)$  in the range specified by the indices  $j$ ,  $k$  and  $n$ . Computing equation 29 therefore requires a convolution for each permutation of  $j$ ,  $k$  and  $n$ . Use of the FFT algorithm prevents the computation of so many convolutions from becoming prohibitively expensive. We will explore the effect of changing the number of convolutions on the accuracy of the model in section 3.3.

## 2.6 Reflection fraction

It is useful to define a reflection fraction that captures the ratio between reflected and direct components in the observed spectrum, specifically isolating geometric considerations from radiative transfer considerations. Here, we discuss two definitions of the reflection fraction: the *system reflection fraction*, which depends only on the geometry of the system and is independent of the observer, and the *observer's reflection fraction*.

The system reflection fraction, already used by the model RELXILLLP (Dauser et al. 2013), is

$$(f_R)_{\text{sys}} = \frac{\cos \delta_{in} - \cos \delta_{out}}{1 + \cos \delta_{out}}, \quad (30)$$

where  $\delta_{in}$  and  $\delta_{out}$  are respectively the values of the angle  $\delta$  for geodesics from the source that hit the inner and outer radii of the disk (Dauser et al. 2014). This definition gives the number of photons that hit the disk divided by the number that reach infinity in the hemisphere above the disk mid-plane. In the case of Newtonian gravity,  $(f_R)_{\text{sys}}$  would reach a maximum of unity for a disk extending from  $r_{in} = 0$  to  $r_{out} = \infty$ . In full GR however,  $(f_R)_{\text{sys}}$  can be much larger due to focusing of photons onto the inner regions of the disk (Dauser et al. 2016).

Although the above definition is conveniently simple, it does not fully capture the relative flux of the direct and

| Parameter                | Units                       | Description   | Default value           |
|--------------------------|-----------------------------|---|-------------------------|
| $h$                      | $R_g$ (+ve) or $R_h$ (-ve)  | Source height   | 6                       |
| $a$                      |                             | Dimensionless spin parameter  | 0.9                     |
| $i$                      | Degrees                     | Inclination angle   | 30                      |
| $r_{in}$                 | $R_g$ (+ve) or ISCO (-ve)   | Disk inner radius   | -1                      |
| $r_{out}$                | $R_g$                       | Disk outer radius   | 20000                   |
| $z$                      |                             | Cosmological redshift   | 0                       |
| $\Gamma$                 |                             | Photon index  | 2                       |
| $\log_{10} \xi$          | $\xi$ has units of erg cm/s | Ionization parameter or peak value of ionization parameter            | 3 or 3.75               |
| $A_{Fe}$                 | Solar                       | Relative iron abundance   | 1                       |
| $(E_{cut})_{\text{obs}}$ | keV                         | Observed high energy cut-off  | 300                     |
| $(kT_e)_{\text{obs}}$    | keV                         | Observed electron temperature   | 300                     |
| $N_h$                    | $10^{22} \text{ cm}^{-2}$   | Hydrogen column density of material in the line-of-sight (TBABS)      | 0                       |
| $1/\mathcal{B}$          |                             | Boosting factor to adjust the reflection fraction from lamppost value | 1                       |
| $M$                      | $M_\odot$                   | Black hole mass   | $4.6 \times 10^7$       |
| $\phi_A$                 | Radians                     | Phase norm - can be self-consistently calculated                      | 0                       |
| $\nu_{\text{min}}$       | Hz                          | Minimum frequency transfer function is averaged over                  | $1 \times 10^{-5}$ or 0 |
| $\nu_{\text{max}}$       | Hz                          | Maximum frequency transfer function is averaged over                  | $2 \times 10^{-5}$ or 0 |
| $\text{ReIm}$            |                             | Sets output   | 1 - 6                   |

**Table 1.** Model parameters for RELTRANS and RELTRANS<sub>CP</sub>. Source height and disk inner radius can be expressed in horizons and ISCOs respectively in order to avoid unphysical parameter combinations during exploration of parameters space. The chosen value of mass corresponds to NGC 4151. The model calculates the energy dependent cross-spectrum averaged over the frequency range  $\nu_{\text{min}}$  to  $\nu_{\text{max}}$ . The parameter  $\text{ReIm}$  sets the model output. The options are: 1) real part, 2) imaginary part, 3) modulus (i.e. the absolute variability amplitude), 4) time lag (the argument divided by  $2\pi\nu$ , where  $\nu = [\nu_{\text{min}} + \nu_{\text{max}}]/2$ ), 5) modulus of the folded cross-spectrum, and 6) the time-lag for the folded cross-spectrum. If either  $\nu_{\text{min}}$  or  $\nu_{\text{max}}$  are set to zero, the time-averaged spectrum is returned.

reflected spectra as seen by a given observer. We therefore additionally define an observer's reflection fraction. In order to exclude the radiative transfer calculation, we define a reflection spectrum for the case in which the disk re-emits the incident spectrum isotropically. In this case, we can define the reflection fraction as the *observed bolometric reflected flux divided by the directly observed bolometric flux*. Note that both of these fluxes are considered to be measured in the *observer's frame*. This means that the specific flux re-radiated from a disk patch is  $F_{d,out}(E_d) = F_{d,in}(E_d)$  (input

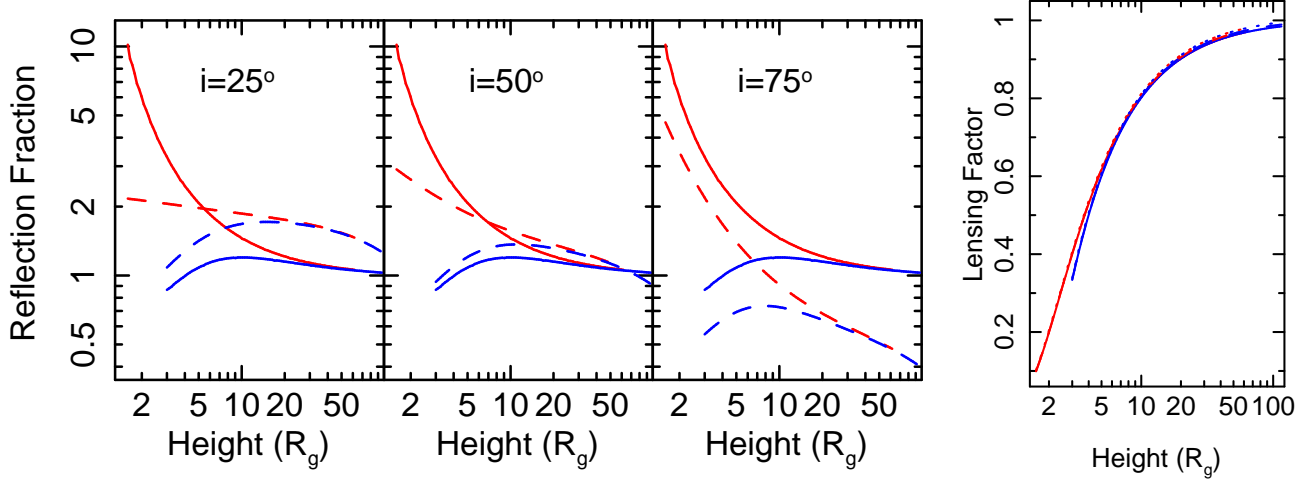


**Figure 3.** *Left:* Reflection fraction plotted against source height for three inclination angles, with the disk extending down to the ISCO for black hole spin  $a = 0.998$  (red) and  $a = 0$  (blue). The solid lines are ‘system’ reflection fraction as defined by Dauser et al. (2016) (see our equation 30) and the dashed lines are the observer’s reflection fraction as defined by our equation 31. The system reflection fraction does not depend on inclination angle whereas the observer’s reflection fraction does, even in the Newtonian limit. *Right:* Lensing factor,  $\ell$ , plotted against source height for  $a = 0.998$  (red) and  $a = 0$  (blue) with  $i = 25^\circ$  (solid),  $i = 50^\circ$  (dashed) and  $i = 75^\circ$  (dotted). We see that  $\ell$  depends very strongly on  $h$ , but only weakly on  $a$  and  $i$ .

spectrum preserved) and the specific intensity re-radiated from the disk patch is  $I_{d,out}(E_d) = F_{d,in}(E_d)/\pi$  (isotropic re-radiation). This gives

$$\begin{aligned} (f_R)_{obs} &= \frac{2}{\ell g_{so}} \int_{\alpha, \beta} g_{do}^3(r, \phi) g_{sd}(r) \frac{|d \cos \delta / dr|}{dA_{ring} / dr} d\alpha d\beta \\ &= \frac{4}{\ell g_{so}} \int_{\alpha, \beta} g_{do}^3(r, \phi) g_{sd}^{1-\Gamma}(r) \epsilon(r) d\alpha d\beta \end{aligned} \quad (31)$$

Applying the earlier experiment of taking the simple limiting case of an infinite slab in Newtonian gravity to equation (31) gives  $(f_R)_{obs} = 2 \cos i$ . Averaging over all  $\cos i$  in the hemisphere above the disk mid-plane, we find  $\langle (f_R)_{obs} \rangle = 1$ ; i.e. source photons are either radiated into the upper hemisphere to be observed directly, or into the lower hemisphere to be observed as reflection. The angular dependence, even when isotropic radiation is assumed, results from the source being a sphere, whereas the disk is a slab. This definition of the reflection fraction is similar, but not identical, to the ‘reflection strength’ defined by Dauser et al. (2016). In our model, we calculate both reflection fractions and print them to screen if the verbose level is set suitably high by an environment variable.

Fig 3 (left) shows our two definitions of reflection fraction plotted against source height for a number of parameter combinations. We see that the solid lines representing  $(f_R)_{sys}$ , which agree exactly with Fig 3 of Dauser et al. (2016), do not depend on viewer inclination. The dashed lines representing  $(f_R)_{obs}$  do depend on viewer position. The right panel shows the contribution of the lensing factor. This is strongly dependent on source height, but only weakly dependent on spin and inclination.

### 3 MODEL PROPERTIES

The model parameters of RELTRANS and RELTRANS<sub>CP</sub> are listed in Table 1. We also define a number of environment

variables, listed in Appendix C, that are used to switch between different modes and control resolution. Each environment variable has a sensible default value, such that the model is user friendly for the beginner and flexible for the advanced user. In this section, we explore the model properties and describe the listed parameters and environment variables. For the sake of intuition we plot time lags and variability amplitudes, even though it is statistically favourable when fitting to data to consider real and imaginary parts of the cross-spectrum (Ingram et al. 2016, 2017; Rapisarda et al. 2017a; Mastroserio et al. 2018).

#### 3.1 Emissivity profiles

Fig 4 shows the lampost model emissivity profile and some contributing factors for a range of parameter combinations. Panel (a) shows the ratio of the area derivative in the Newtonian case to the relativistic case for three different values of spin. The difference between the three spin values results entirely from the Lorentz factor of the rotating disk element,  $\gamma^\phi$ . This plot is very similar, but not identical, to the corresponding plot in Dauser et al. (2013) (top panel in their Fig 2). The discrepancy results from small (inconsequential as it turns out) mistakes in the expressions for  $\gamma^\phi$  in Bardeen et al. (1972) (equation 13.12a) and Dauser et al. (2013) (equation 10). The two expressions are identical *except* the latter reference drops all  $\pm$  and  $\mp$  signs, meaning that they agree for prograde spin but differ slightly for retrograde spin. Upon further investigation, detailed in Appendix A, we found a very subtle mistake in equation (13.12a) of Bardeen et al. (1972), which is again very small and only relevant for retrograde spin. We find that, for  $a = -0.99$  (which maximises the magnitude of the error), the Dauser et al. (2013) version actually gives a closer answer to our new expression than the Bardeen et al. (1972) version, although all three are very similar.

Panel (b) shows the contribution of the blueshift factor

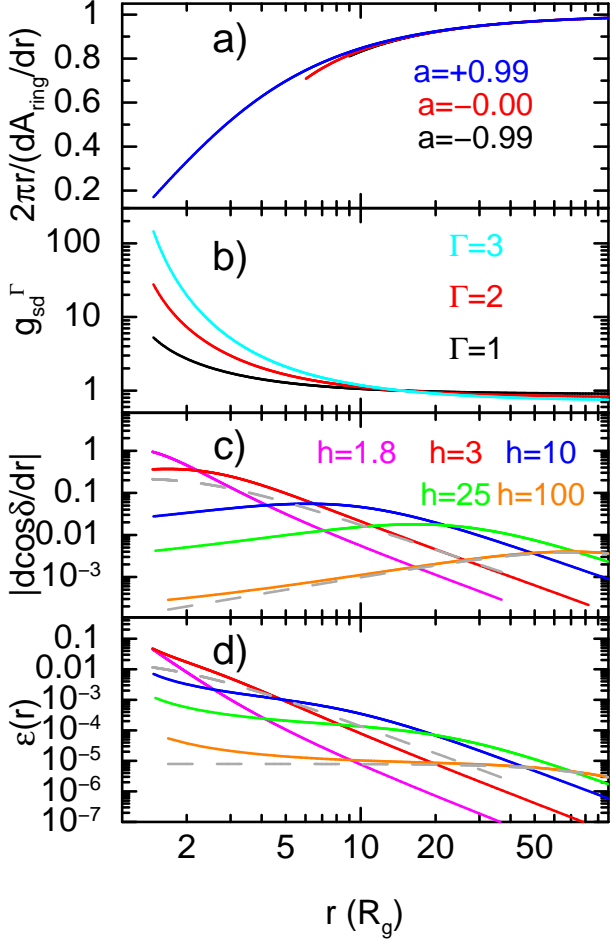


**Figure 4.** Contributions to the radial emissivity profile, designed for comparison to Fig 2 in Dauser et al (2013). *a*: Ratio of the Newtonian radial derivative to the fully relativistic version for spin as labelled. *b*: Contribution to the emissivity of the blueshift factor for  $h = 10$  and  $a = 0.99$ . *c*: Radial derivative of  $\cos \delta$  for  $a = 0.99$  and  $h$  as labelled. The grey dashed lines are the Newtonian equivalent for  $h = 1.8$  (to be compared with the solid magenta line) and  $h = 100$  (to be compared with the solid orange line). As expected, this is a better approximation for larger source heights. *d*: Emissivity profile for  $\Gamma = 2$ ,  $a = 0.99$  and  $h$  as labelled in panel *c*. Again, the grey dashed lines are the Newtonian equivalent [ $\epsilon(r) \propto (h^2 + r^2)^{-3/2}$ ] for  $h = 100$  and  $h = 1.8$ .

for three different values of  $\Gamma$ , illustrating that a steeper spectrum leads to a steeper emissivity profile. Panels (c) and (d) show respectively the radial derivative of the cosine of the angle  $\delta$  and the overall emissivity profile for various parameter combinations. The grey dashed lines represent the Newtonian approximations [ $|d \cos \delta / dr| = hr(h^2 + r^2)^{-3/2}$  and  $\epsilon(r) = h(h^2 + r^2)^{-3/2} / (4\pi)$ ] for  $h = 1.8 R_g$  (to be compared with the magenta lines) and  $h = 100 R_g$  (to be compared with the orange lines). We see that, as expected, the full GR solution diverges dramatically from the Newtonian approximation for low source heights. Our emissivity profiles agree with those presented in Dauser et al. (2013).

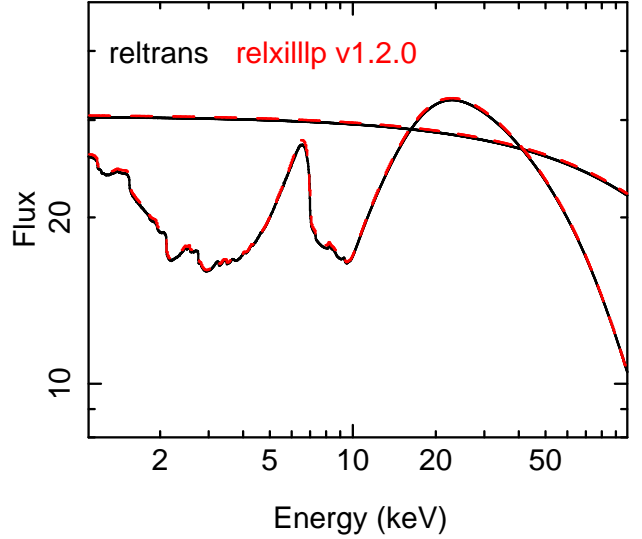


**Figure 5.** Time-averaged direct and reflected spectrum for RELTRANS (black), and the most recent version of RELXILLLP (red, dashed). We see good agreement between the two models.

### 3.2 Time-averaged spectrum

Fig 5 shows the direct and reflected components of the time-averaged spectrum calculated by RELTRANS (black) and the most recent version of RELXILLLP at the time of writing (red, dashed). We use the default parameters listed in Table 1, except we set  $r_{out} = 400 R_g$  for ease of comparison with RELXILLLP. RELXILLLP accounts for the dependence of emission angle and disk rest frame cut-off energy on disk coordinates, but assumes a single ionization parameter. For the purposes of comparison in this plot, we therefore follow suit (although see sections 3.3.1 and 3.3.2 for further discussion on these dependencies), and use the default number of zones for both  $\mu_e$  and  $E_{cut}$ . For all models, the relative normalisation of reflected and direct components is calculated self-consistently, rather than set as a model parameter. We see that RELXILLLP agrees very well with our model<sup>4</sup>. Besides benchmarking against RELXILLLP, we have also thoroughly tested our code by comparing it with outputs calculated using brute-force calculation of the transfer function (i.e. without using the kernel convolution).

### 3.3 Rest frame assumptions

In this section, we explore the impact of accounting for the coordinate dependence of the emission angle and high energy cut-off (3.3.1) and ionization parameter (3.3.2), before comparing RELTRANS to RELTRANS<sub>CP</sub> (3.3.3).

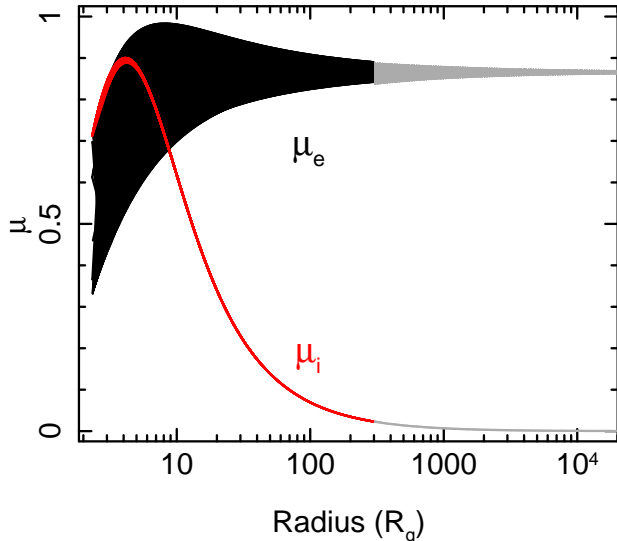


**Figure 6.** Cosine of the emission angle (black) and incidence angle (red) as a function of radius for the default parameters ( $i = 30^\circ$ ). We see that the emission angle depends on azimuth as well as radius, whereas the incidence angle is a monotonic function of radius. The grey points at  $r \gtrsim 400 R_g$  are computed assuming that rays travel in straight lines. The smooth joins from the full GR treatment used for  $r \lesssim 400 R_g$  demonstrate that this is a reasonable assumption.

### 3.3.1 Emission angle and cut-off energy

Fig 6 shows the radial dependence of the cosine of the emission angle,  $\mu_e$ , for the default parameters, with the spread being for different disk azimuths. As expected,  $\mu_e \approx \cos(i)$  for very large disk radii, but covers an enormous range for smaller disk radii. The RELXILL family of models for the time-averaged spectrum (García et al. 2014) account for this disk coordinate dependence of the emission angle, and now also for the radial dependence of apparent  $E_{cut}$  observed in the disk rest frame. Here, we investigate both effects in the context of the timing properties. Fig 7 shows the time-averaged spectrum (a), time lags (b) and variability amplitude (c) calculated for  $i = 30^\circ$  (left) and  $i = 80^\circ$  (right). The different lines account for neither effect (black), only emission angle (red), only cut-off energy (green) and both effects (blue). For the purposes of the variability amplitude calculation, we simply set  $\alpha(v) = 1$  (this in itself is unphysical, corresponding to 100% fractional variability, but as an arbitrary constant it does not have any bearing on our analysis). We see that the  $E_{cut}$  effect is always subtle, but the emission angle effect can become very large for high inclination angles (consistent with what García et al. 2014 found for the time-averaged spectrum). These figures use 10 zones to account for both effects, which we find to be comfortably enough to reach convergence for all trialled parameter combinations. Since acceptable accuracy can be achieved by using as few as 5 zones for both quantities, we set 5 as the

<sup>4</sup> Model versions of RELXILLP prior to v1.2.0 have a smaller relative normalization of the reflection spectrum. This comes partly from an extra factor of  $0.5 \cos i$  that is applied to the XILLVER spectrum before being convolved with the smearing kernel in the older versions

default value for the environment variables MU\_ZONES and ECUT\_ZONES (see Table C1). The user can adjust these values to test for convergence.

### 3.3.2 Ionization profile and incidence angle

The ionization parameter is proportional to the 13.6 eV to 13.6 keV illuminating flux,  $F_x(r) \propto g_{sd}^{2-\Gamma}(r)\epsilon(r)$ , divided by the disk electron density  $n_e(r)$ . Whereas the flux is known exactly in the lamppost model,  $n_e(r)$  is more uncertain. Shakura & Sunyaev (1973) define equations for 3 disk zones, where zone A is the innermost region, in which pressure is dominated by radiation and the opacity is dominated by electron scattering. Since the emissivity is dominated by the inner regions, we first investigate the zone A density profile (equation 2.11),  $n_e(r) \propto \alpha^{-1} r^{3/2} [1 - (r_{in}/r)^{1/2}]^{-2}$ , where  $\alpha$  is the viscosity parameter [not to be confused with our normalisation parameter  $\alpha(v)$ ]. The density profile is very different for the other zones at larger radii, but for these radii  $F_x$  is small and so the predicted ionization is small regardless of the assumed density profile. The black solid line in Fig 8 shows the resulting ionization profile for the default parameters. For simplicity, we have taken the viscosity parameter to be a constant, but we stress there is no *a priori* reason to assume this. There are other reasons to suspect an alternative density profile. For instance, the stress-free inner boundary condition may not be appropriate for a truncated disk, or there may be no zone A present when the accretion rate is a small fraction of the Eddington limit. We therefore additionally explore the simplest possible case of constant density (following Svoboda et al. 2012). The resulting ionization profile is plotted in Fig 8 (black dashed line).

We normalise the ionization profile by specifying as a model parameter the peak ionization value,  $\log_{10} \xi_{max}$ . For the constant density model, the peak simply occurs at the disk inner radius. For the zone A density profile, we use  $r_{peak} = (11/9)^2 r_{in}$ , which is only exact for  $\epsilon(r) \propto r^{-3}$ , but numerical calculation of the exact  $r_{peak}$  would be fairly expensive for no real gain.

Another effect to consider is the radial dependence of the incidence angle of illuminating photons  $\delta_i$  (see Fig 2), the cosine of which is plotted for the default parameters in Fig 6 (red line). The incidence angle influences the shape and normalisation of the restframe reflection spectrum (García & Kallman 2010) but, in order to save computational expense, the public XILLVER grid is tabulated only for  $\delta_i = 45^\circ$ . Since the leading order effect is on the intensity of the radiation field at the disk upper boundary,  $2F_x(r)/\mu_i(r)$ , the radial  $\mu_i$  profile can be approximately accounted for very cheaply by adjusting the ionization profile (García & Kallman 2010; Dauser et al. 2013). The red lines in Fig 8 show the logarithm of the ‘effective’ ionization parameter,  $\xi_{eff}(r) = \xi(r) \cos(45^\circ)/\mu_i$ , that results from this adjustment. We use this effective ionization in our model since it captures more physics for no extra computational cost.

Figs 9 and 10 show the time-averaged spectrum (a), time lag (b) and amplitude (c). The thick black lines are computed for a single ionization parameter of  $\log_{10} \xi = 3$ , whereas a self-consistently calculated effective ionization profile has been used for the coloured lines. We use the zone A density profile for Fig 9 and constant density for Fig 10. From bottom to top, the red, green, blue, cyan and magenta

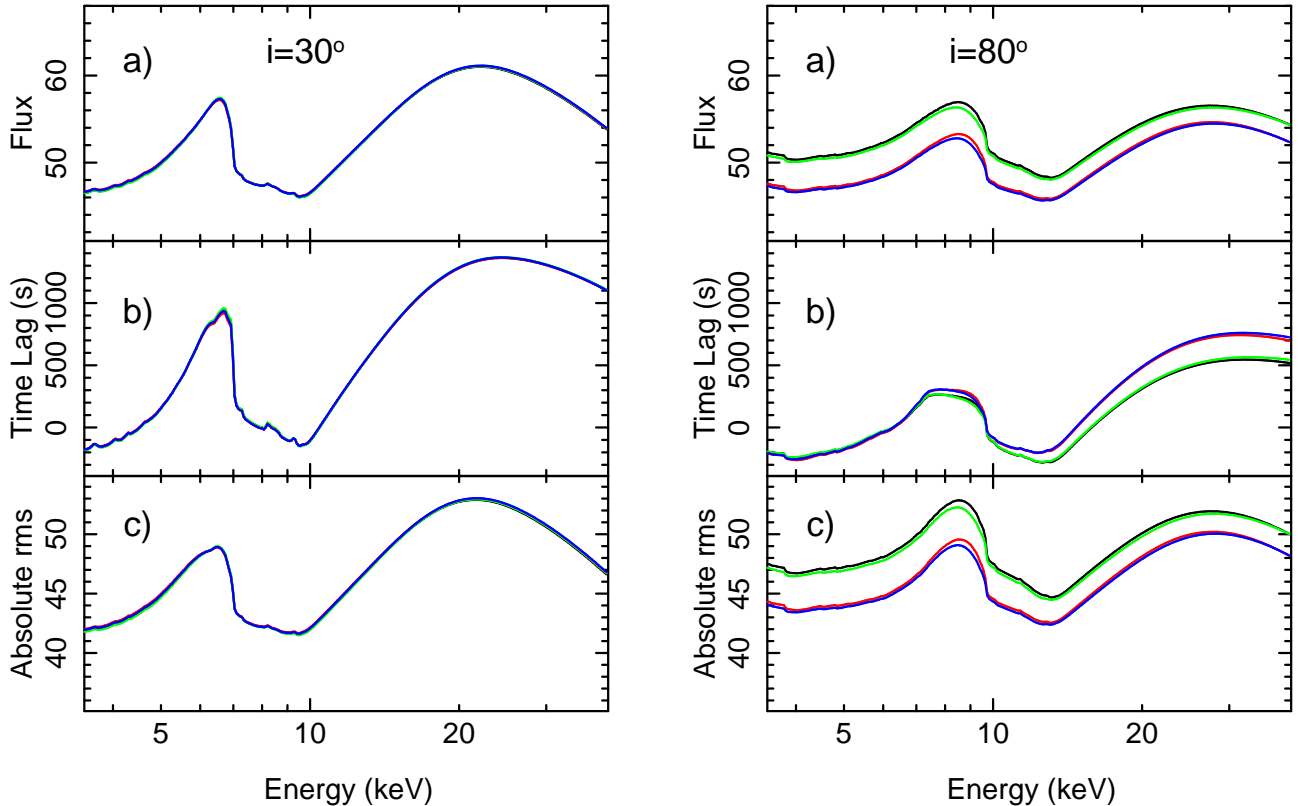


**Figure 7.** RELTRANS time-averaged spectrum (a),  $1 - 2 \times 10^{-5}$  Hz time lags (b) and absolute variability amplitude (c) calculated for the default parameters. Left and right hand panels correspond to inclination angles of  $30^\circ$  and  $80^\circ$  respectively. For the black lines, we set the emission angle  $\delta_e$  equal to the inclination angle  $i$  and ignore the radial dependence of  $E_{cut}$  as measured in the disk restframe. For the other lines, we account only for the disk coordinate dependence of  $\mu_e$  (red), only for the  $E_{cut}$  dependence (green), and for both (blue). A single ionization parameter is used. For the lags,  $\phi_A$  is calculated for a 2–10 keV *XMM-Newton* EPIC pn reference band flux.

lines are for  $\log_{10} \xi_{max} = 3, 3.5, 3.75, 4.0$  and  $4.25$  respectively. We see that this modification to the model makes an enormous difference to all outputs. For the zone A profile, setting  $\log_{10} \xi_{max} = 3.75$  (blue lines) gives the closest match to the constant ionization model in terms of the relative peak fluxes of the time-averaged iron line and reflection hump. However, the red wing of the iron line is much more prominent for the self-consistent case. The constant density case is similar, except for  $\log_{10} \xi_{max} = 4.25$ . We will investigate possible biases that this may cause when fitting constant ionization models to observational data in section 4.2. The effect is even greater if we also consider the timing properties. The self-consistent models have smaller iron line lags than the single ionization model, which may perhaps be mistaken for the source height or disk inner radius being smaller. The absolute rms spectrum shows that the iron line is much more variable for the self-consistent case. As we will see in section 4.2, it is possible to choose a value of  $h$  that allows the single ionization model to mimick the time-averaged spectrum of the self-consistent case, but the different effect that the ionization gradient has on the timing properties means that considering also time lags and variability amplitude breaks the degeneracy. Both figures here are plotted using 100 zones in ionization parameter. We find however that reasonable convergence can be achieved for 10 zones, and so we set this as the default value for the `ION_ZONES` environment variable (see Table C1).

### 3.3.3 reltransCp vs reltrans

Fig 11 demonstrates typical differences between RELTRANS (black lines) and RELTRANS CP (red lines). Whereas the former uses an exponentially cut-off power-law for the illuminating spectrum, the latter uses the model NTHCOMP (Zdziarski et al. 1996; Źycki et al. 1999), which gives a much better approximation of Compton up-scattering of seed photons by a thermal population of hot electrons. We see that NTHCOMP has a low energy cut-off, which is determined by the seed photon temperature  $kT_{bb}$ . In the XILLVERCP tables, this is hardwired to 0.05 keV (assuming a multi-temperature blackbody spectrum of seed photons). The shape of the high energy cut-off is also very different for NTHCOMP. The difference between the two models is small for the lags though. Since RELTRANS CP employs a more physical emission model for little extra computational expense, we use it for the remainder of the plots in this paper.

### 3.4 Frequency dependence

Fig 12 demonstrates the frequency dependence of RELTRANS CP for the default parameters. Panel a shows the phase normalisation  $\phi_A(v)$  calculated for a 2–10 keV reference band measured by the EPIC-pn instrument onboard the *X-ray Multi-mirror Mission* (*XMM-Newton*; Jansen et al. 2001) in timing mode (calculated from equation 25). As noted in Mastroserio et al. (2018), we can only be confident that this

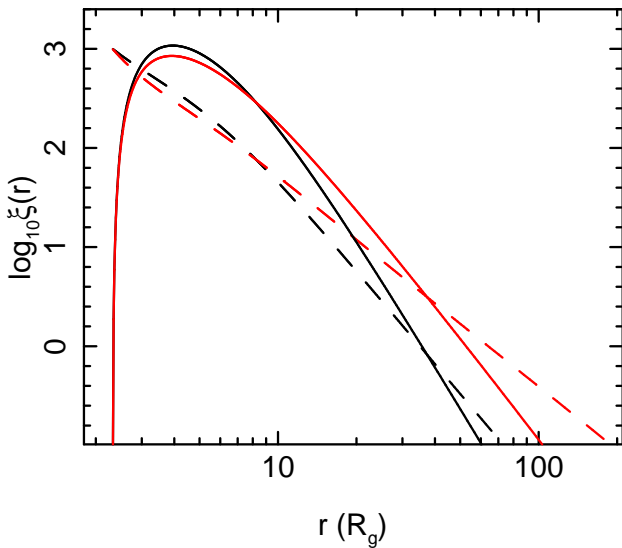


**Figure 8.** The black lines are radial ionization profiles calculated assuming a zone A density profile (solid) and constant density (dashed). The red lines are effective ionization profiles, which have been adjusted to account for the radial dependence of the incidence angle.

function is a correct representation of the underlying spectral model if all the channels used for the reference band are considered to be well calibrated. The range 2–10 keV demonstrated in the plot is well calibrated for *XMM-Newton*. If for any reason we wish to define our reference band from poorly calibrated channels, for instance if we wish to maximize signal to noise by collecting more photons, then a systematic error will be introduced into the calculation of  $\phi_A(v)$  because the instrument response matrix used for the calculation does not adequately describe the true response of the telescope for all energy channels. In such a case, it may be best to leave  $\phi_A(v)$  as a free parameter for each frequency range considered, although this will inevitably lead to larger statistical errors.

Panels b and c show respectively time lags and absolute variability amplitude as a function of energy for 10 different frequency ranges. The overall lag reduces and the iron line feature gets broader with increasing frequency because the higher frequencies select reflection from smaller regions of the disk. Similarly, the line feature in the rms spectrum becomes weaker for higher frequencies as the fastest variability is washed out by path length differences introduced by reflection from different parts of the disk. At the highest frequency range plotted here, we see the effects of phase-wrapping, evidenced by the iron line and reflection hump becoming dips as opposed to excesses in the rms spectrum.

Our model calculates the energy dependent cross-spectrum for a given frequency range, rather than the cross-spectrum as a function of frequency for a given energy range. This feature is hardwired because we calculate the energy dependent transfer function in Fourier space (see equation 22) for a range of frequencies between  $\nu_{min}$  and  $\nu_{max}$ . This is much more computationally efficient than first calculating a 2D impulse-response function and Fourier transforming the time axis. All frequencies can be taken into account by fitting for many frequency ranges, as in Mastroserio et al. (2018).

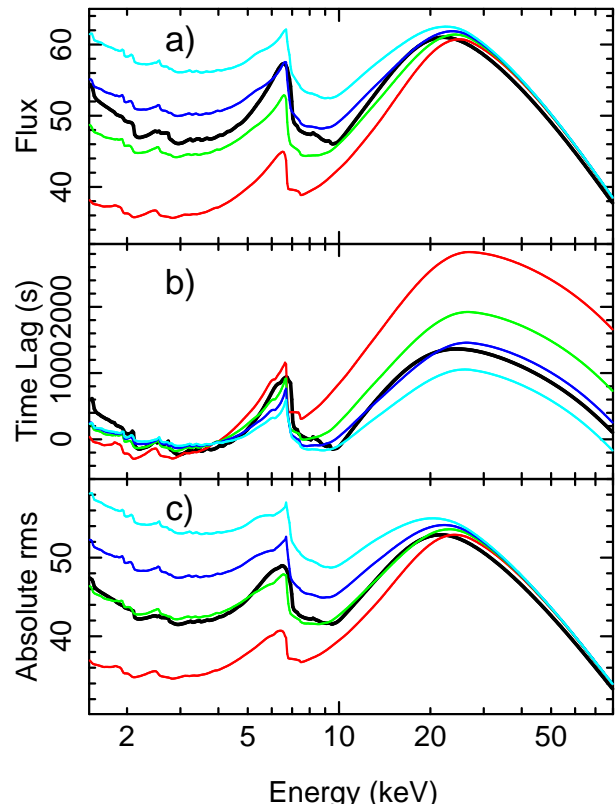


**Figure 9.** RELTRANS time-averaged spectrum (a), time lags (b) and absolute variability amplitude for different assumptions regarding the radial ionization profile. For all lines, we assume the default parameters, and for the time lag we assume that the reference band was the 2–10 keV EPIC-pn flux. For simplicity, we ignore the  $\mu_e$  and  $E_{cut}$  dependencies explored in Fig 7. The thick black lines are for a constant disk ionization parameter,  $\log_{10}\xi = 3.0$ . The other lines assume a radial ionization profile self-consistently calculated from the emissivity profile and the density profile relevant to Shakura and Sunyaev’s zone A. From bottom to top, the red, green, blue and cyan lines assume a ‘peak’ ionization of  $\log_{10}\xi = 3, 3.5, 3.75, 4.0$ . We see that accounting for the radial ionization profile makes an enormous difference to the results.

The public model does not currently include non-linear effects, but will soon be updated (description in Mastroserio et al submitted). Intrinsic hard lags can alternatively be produced by summing two model components. This is only possible when considering real and imaginary parts of the cross-spectrum, and the phase normalisations of the two component must be free parameters (i.e. not self-consistently calculated) and independent of one another. Using, for example, two RELTRANS components with different source heights and different spectral indices is the same as assuming the ‘two blobs’ geometry of Chainakun & Young (2017). The Fourier frequency dependent propagation time between the blobs is simply  $|\phi_{A1}(v) - \phi_{A2}(v)|/(2\pi v)$ .

#### 4 MODELLING BIASES

In this section, we explore two sources of bias in previous treatments of reflection and reverberation in the literature. The first is ignoring the instrument response matrix when

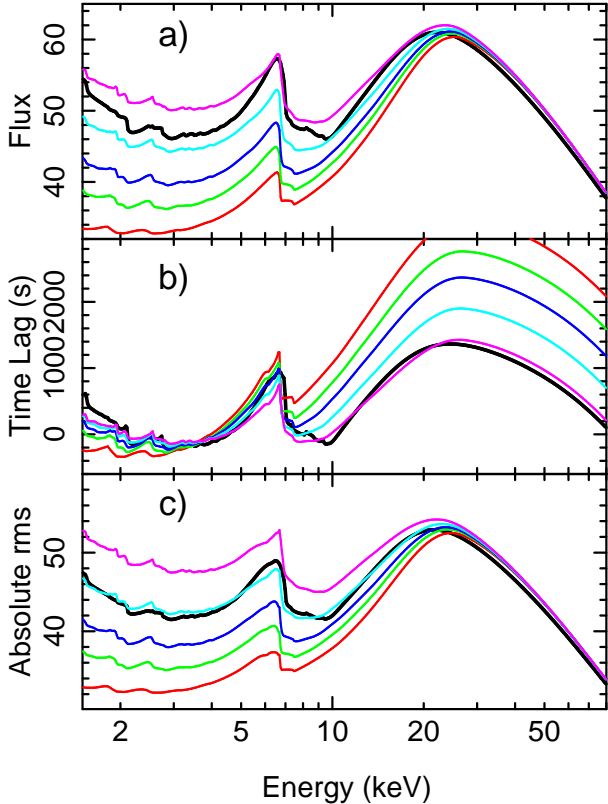


**Figure 10.** Same as Fig 9, except the radial ionization profile is calculated assuming a disk with constant density. The magenta lines are for  $\log \xi(r_{in}) = 4.25$ . For this constant density case, the peak ionization that most closely matches the spectrum to the constant ionization case is slightly higher (i.e. 4.25, magenta line). We again see that the red wing of the iron line in the time-averaged spectrum (a) is exaggerated compared with the constant ionization model (thick black lines), even though the change in shape of the line is slightly less dramatic than for Fig 9. The use of a self-consistent ionization profile again has a significant affect on the time lags (b) and absolute rms (c), with the self-consistent ionization profile again leading to a more variable iron line (see magenta lines).

analysing time lags. In section (4.1), we show that the value of the lag can be heavily biased in an energy range for which the instrument response is not diagonal and in which line-of-sight absorption is prominent. This is because such an energy range is *dominated* by photons from other energy bands that have been ‘mis-classified’. The other source of bias is assuming a single disk ionisation parameter instead of accounting for a self-consistently calculated radial ionisation profile (section 4.2).

#### 4.1 Bias caused by ignoring the telescope response

Our model provides two ways to properly account for the instrument response and line-of-sight absorption. The recommended option for the purposes of fitting to data is to consider the real and imaginary parts of the cross-spectrum ( $\text{ReIm}=1$  and 2). In this case, the fits files containing the data can be read into XSPEC in the normal way, with response files specified in the header, and the usual XSPEC operation

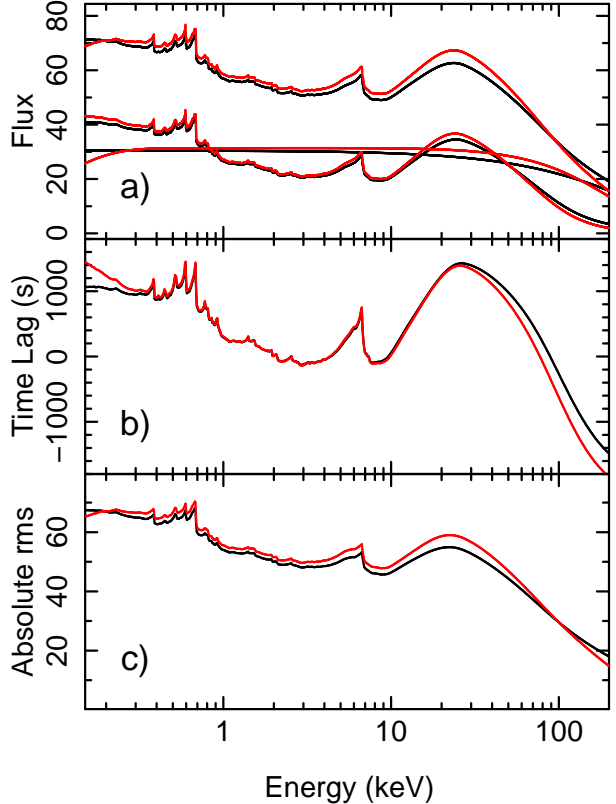


**Figure 11.** Time-averaged spectrum (a), time lags (b) and absolute variability amplitude calculated from the default parameters. The black lines represent the model RELTRANS (which assumes an exponentially cut-off power-law for the direct spectral component) and the red lines represent RELTRANS CP (which uses NTHCOMP for the direct spectrum). We see a significant difference in the time-averaged direct component. The time lags are largely unaffected for energies below  $\sim 20$  keV, whereas the more physical model RELTRANS CP predicts a larger variability amplitude. Here we use default values for the environment variables, and the phase zero point is self-consistently calculated for a 2 – 10 keV *XMM-Newton* pn timing mode reference band.

of folding around the instrument response is appropriate. The user can then plot the best fitting cross-spectral model in terms of variability amplitude and time lags after the fit is complete ( $\text{ReIm}=3$  and 4). However, the user may wish to instead fit for time lags and/or variability amplitude. In this case, the model cross-spectrum is folded around the instrument response within the code and the variability amplitude and time lags are calculated from this folded cross-spectrum ( $\text{ReIm}=5$  and 6). Observationally constrained time lags and rms can be loaded into XSPEC with a diagonal dummy response matrix (using e.g. `f1x2xsp`). The response files can be set through environment variables (`RMF_SET` and `ARF_SET`). If the environment variables are not set but the code is in a mode requiring a response, the user will instead be prompted at the terminal for input.

Fig 13 illustrates the importance of correctly accounting for the instrument response. The black line represents time lags for the model only, ignoring the instrument response (i.e.  $\text{ReIm}=4$ ). In this case, the absorption model is not relevant because it cancels out when the imaginary part of the cross-spectrum is divided by the real part. The red line rep-

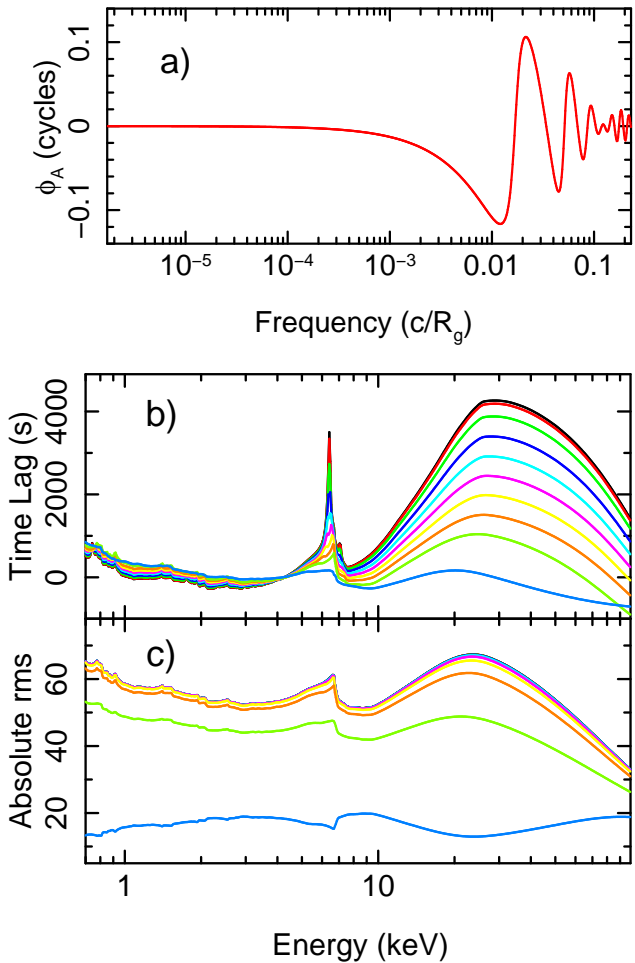


**Figure 12.** *a:*  $\phi_A(\nu)$  calculated using the default model parameters of RELTRANSCP (default environment variables), assuming that the reference band is the 2–10 keV EPIC-pn flux. *b:* Time lag versus energy for the same parameters using the same calculation for  $\phi_A(\nu)$ . The black, red, green, blue, cyan, magenta, yellow, orange, light green and light blue lines (top to bottom) are calculated for different frequency ranges, which increase logarithmically from a minimum of  $10^{-8}$  Hz to a maximum of  $10^{-4}$  Hz (this range corresponds to  $0.046$ – $460$  Hz for a  $10M_\odot$  black hole, or  $\sim 2.26 \times 10^{-6}$ – $10^{-2}$   $c/R_g$ ). *c:* The same calculation but for variability amplitude, setting  $\alpha(\nu) = 1$ .

resents the same model, but now the EPIC pn response has been used and we set the hydrogen column density to  $N_h = 0$ . The blue dashed line is the same again except that now we set  $N_h = 10^{22} \text{ cm}^{-2}$ . We see very little differences in the 2–10 keV region, whereas above  $\sim 15$  keV the lags are completely undefined due to lack of effective area. The differences between the lines below  $\sim 1$  keV occur because the response matrix is not diagonal in this energy range. For  $N_h = 0$ , the resulting ambiguity between soft photons and harder photons ‘mis-classified’ as soft simply smears out sharp features. When absorption is taken into account, the soft band instead becomes *dominated* by the mis-classified photons. This essentially introduces dilution: the lag between 0.5 and 1 keV is very small because most of the photons recorded in the  $\sim 0.5$  keV channel are actually  $\sim 1$  keV photons.

Whereas Fig 13 is relevant for high frequencies at which

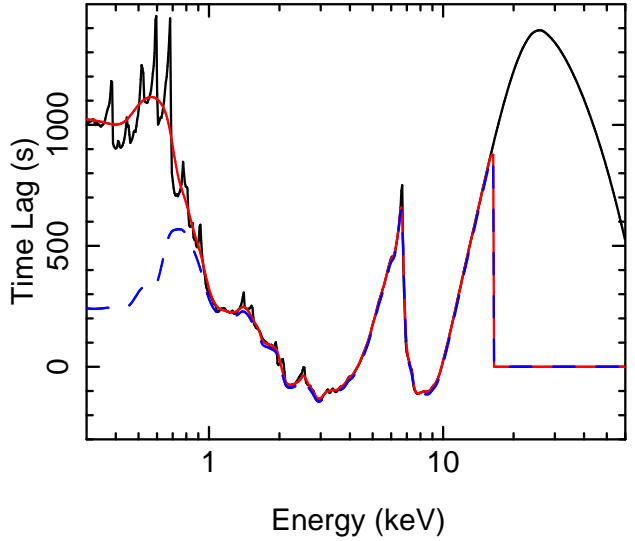


**Figure 13.** Time lags calculated for the default parameters. The black line is for the model only, and so does not account for a telescope response matrix. The red and blue lines assume the pn response and absorption column densities of  $N_h = 0$  and  $10^{22} \text{ cm}^{-2}$  respectively. We calculate  $\phi_A$  for all three assuming the reference band is the 2–10 keV band of the pn.

the reverberation lags dominate over the intrinsic hard lags, the same effect is also potentially important for lower frequency ranges in which the intrinsic lags are still significant. In particular, signatures of thermal reverberation have been detected for a number of black hole X-ray binaries including GX 339-4 (Uttley et al. 2011; De Marco et al. 2017). In the 1–30 Hz frequency range, log-linear intrinsic lags are seen for  $E \gtrsim 1$  keV and a turn up is seen for  $E \lesssim 1$  keV, which is attributed to thermal reverberation (see top right of Fig 7 in De Marco et al. 2017). We investigate how this thermal reverberation signal may have been affected by the instrument response by first assuming that the intrinsic lag spectrum in the 1–30 Hz frequency range is simply log-linear for the full energy range (Fig 14, black line). From this, we calculate the energy dependent cross-spectrum. This additionally requires a model for the time-averaged spectrum and a model for the energy dependent fractional variability amplitude. We use TBABS\*NTHCOMP ( $N_h = 6 \times 10^{-21} \text{ cm}^{-2}$ ,  $\Gamma = 1.9$ ,  $kT_{bb} = 0.18$  keV) for the time-averaged spectrum and assume that the fractional rms increases linearly with energy ( $\text{rms} \propto 0.024E + 0.043$ , although our results only depend very weakly on this function). We then fold our model cross-spectrum around the *XMM-Newton* pn timing mode response matrix and calculate the ‘folded’ lag spectrum from the argument of this folded cross-spectrum (red line). We see a clear turn up in the ‘folded’ lag spectrum below  $\sim 1$  keV that results from these energy channels being dominated by ‘mis-classified’ photons.

On first inspection, this looks worryingly like a spurious signature of thermal reverberation. However, the observation of GX 339-4 that our model is based upon has a number of characteristics that convincingly point to the presence of thermal reverberation. In particular, De Marco et al. (2017) present the 5–30 Hz lag energy spectrum in their Fig 7. That the  $\sim 0.5$  keV lag increases as progres-

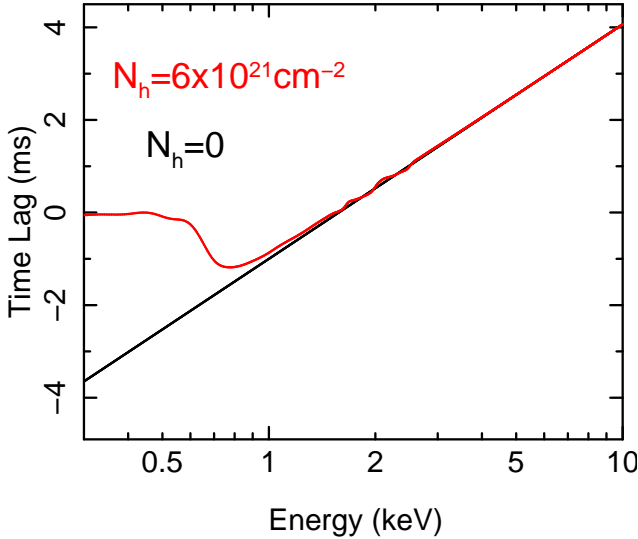


**Figure 14.** Log-linear time lag as a function of energy (black), with the parameters chosen to roughly match the 1 – 30 Hz lag spectrum of GX 339-4 in observation ‘OI’ from De Marco et al. (2017) and Mahmoud et al. (2018). The red line is the time lag that would be observed by *XMM-Newton* assuming that the intrinsic lag-energy spectrum is given by the black (log-linear) line. To calculate this, we take the argument of the absorbed and folded model cross-spectrum. We see that an intrinsically log-linear lag spectrum appears to turn up at  $E \lesssim 1$  keV in *XMM-Newton* observations.

sively higher frequency ranges are chosen is very suggestive of thermal reverberation. Moreover, the  $E \sim 0.5$  keV lag is larger than the lag in the  $\sim 1$  – 6 keV energy range, and so simply cannot be caused by the instrumental effect that we have explored here - which can only dilute the soft lags by averaging with the higher energy lags. We therefore conclude that the thermal reverberation interpretation of the data is sound. However, the *value* of the lag is very likely biased by the instrument response. In particular, Mahmoud et al. (2018) fit a transfer function model to the data that only accounts for the effective area curve of the instrument but not the redistribution matrix. This implies that the true reverberation lags are shorter than originally thought, and the measured disk inner radius of  $\sim 20 R_g$  may reduce once the correction is made.

We conclude that it is important to properly account for the telescope response matrix when modelling the  $\lesssim 1$  keV region of *XMM-Newton* data, either by fitting for real and imaginary parts, or using the folding option. A similar effect is present in the *NICER* response, but not that of the *Nuclear Spectroscopic Telescope ARray* (*NuSTAR*; Harrison 2013).

## 4.2 Bias caused by using a single ionization

It is clear from the discussion in Section 3.3, and in particular Figs 9 and 10, that including a self-consistent radial ionization profile can give very different model outputs to simply assuming a constant ionization parameter. In this section, we create a fake *NuSTAR* time-averaged spectrum and fit back with a single ionization parameter model in order to investigate biases that may have been introduced

| Parameter                           | Input | Control Fit                 | Single Ion Fit              |
|-------------------------------------|-------|-----------------------------|-----------------------------|
| $N_H$ ( $10^{22} \text{ cm}^{-2}$ ) | 1     | 1                           | 1                           |
| $h$ ( $R_g$ )                       | 6     | $5.48^{+0.616}_{-0.546}$    | $2.45^{+0.26}_{-0.26}$      |
| $a$                                 | 0.9   | $0.99^{+0.009}_{-0.009}$    | $0.778^{+0.0461}_{-0.0581}$ |
| $i$ (degrees)                       | 30    | $30.7^{+1.06}_{-1.72}$      | $29.1^{+0.89}_{-1.12}$      |
| $\Gamma$                            | 2     | $2.0^{+0.01}_{-0.01}$       | $2.03^{+0.015}_{-0.009}$    |
| $\log_{10} \xi^*$                   | 3.75  | $4.13^{+0.289}_{-0.587}$    | $3.05^{+0.034}_{-0.034}$    |
| $A_{Fe}$                            | 1     | $0.967^{+0.1926}_{-0.1259}$ | $0.999^{+0.1198}_{-0.0599}$ |
| $(kT_e)_{obs}$ (keV)                | 50    | $46.1^{+15.0}_{-5.37}$      | $50.8^{+11.81}_{-3.23}$     |
| $1/\mathcal{B}$                     | 0.5   | $0.571^{+0.1694}_{-0.0743}$ | $0.419^{+0.0511}_{-0.0188}$ |
| norm ( $10^{-2}$ )                  | 10    | $7.97^{+0.959}_{-0.621}$    | $56.8^{+4.86}_{-12.51}$     |
| XILLVERCP norm ( $10^{-3}$ )        | 0     | 0                           | $6.32^{+0.08}_{-0.078}$     |
| $\chi^2/\text{d.o.f.}$              |       | 1540.68/1561                | 1505.89/1560**              |

**Table 2.** Input parameters and values measured by fitting back with the correct (control) model and a single ionization model. Errors are 90% confidence limits, and  $p$  denotes that the parameter is pegged at a hard limit. \*The ionization parameter has different meanings in the two models (single value vs maximum value). \*\* A 0.5% systematic error was applied for the single ionization model fit, as is commonly practiced in spectral fitting to account for calibration uncertainty and model systematics. Without the systematic error, the best fitting single ionization model has a reduced  $\chi^2$  of 1626.38/1560, corresponding to a goodness of fit that is common for fits to real *NuSTAR* spectra (e.g. Miller et al. 2013).

into the many spectral fitting studies that have used a single ionization model.

### 4.2.1 Fake data

We simulate a 30 ks *NuSTAR* observation of a bright X-ray binary by inputting the model parameters listed in Table 2 into RELTRANS<sub>CP</sub>, with the normalisation set to roughly match the observed flux of GX 339-4 when  $\Gamma \approx 2$  (model 4 – 10 keV flux =  $5 \times 10^{-9}$  erg  $\text{cm}^{-2} \text{ s}^{-1}$ ). We use FAKEIT to generate a fake 30 ks FMPA exposure, taking background into account. We ignore deadtime effects, but do not generate an FPMB exposure. Statistically, this is the same as taking both focal plane modules into account and assuming a deadtime correction factor of 1/2. Our fake observation therefore corresponds to a typical high quality observation used for the purposes of spectral fitting (e.g. Parker et al. 2015; Xu et al. 2018; Tomsick et al. 2018). We only simulate the time-averaged spectrum, since there have thus far only been a few studies fitting reverberation models to timing data.

Our input model assumes the Zone A Shakura-Sunyaev density profile. This is a reasonable assumption for the brightest hard / hard intermediate states of X-ray binaries. The bolometric luminosity of GX 339-4 is  $L_x \sim 10^{38.5}$  erg  $\text{s}^{-1}$  when  $\Gamma = 2$  (see Fig 5 of Plant et al. 2014). For  $M \lesssim 10 M_\odot$  (Heida et al. 2017) and a viscosity parameter  $\alpha \gtrsim 0.01$ , the zone A to B transition is therefore at  $r_{ab} \gtrsim 200 R_g$  (equation 2.17 in Shakura & Sunyaev 1973), indicating that the

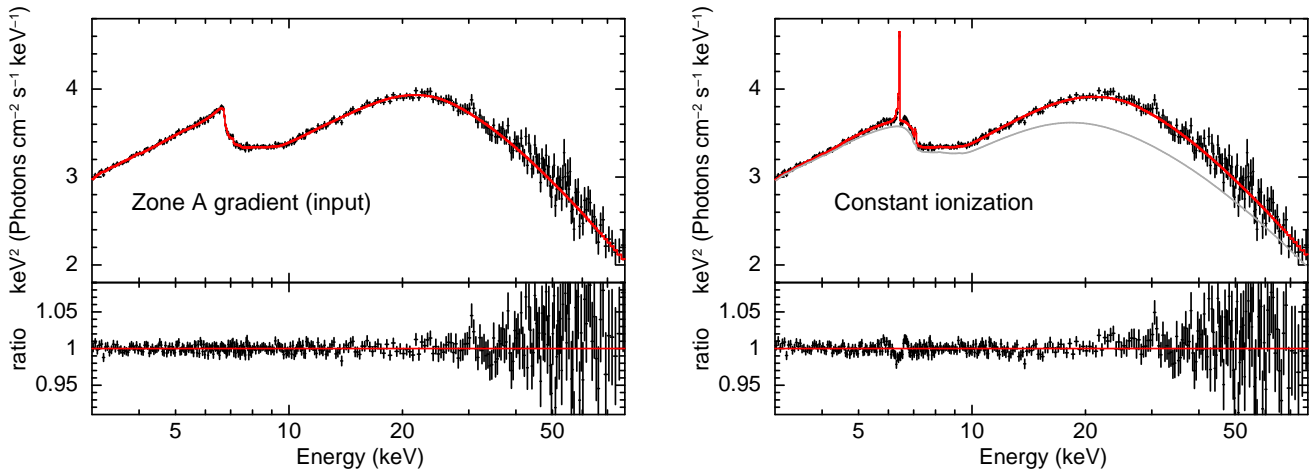


**Figure 15.** Unfolded fake data and model (top) and fake data to model ratio (bottom). The data were generated from a model with a radial ionization profile calculated assuming a zone A Shakura-Sunyaev density profile. Left and right hand plots respectively show the results of fitting the input model and an alternative model with a single ionization parameter (red) plus an extra XILLVER component (grey). Results are further detailed in Table 2. Spectra have been re-binned for plotting purposes (binned to a target signal to noise ratio of 150 but not co-adding more than 10 channels).

region of the disk that dominates the emissivity is radiation pressure and electron scattering dominated. Following the discussion in section 3.3 concluding that the disk coordinate dependence of  $\mu_e$  and disk rest frame observed electron temperature are not important for low source inclinations, we use 100 ionization zones for our input model, and only one for the emission angle and electron temperature.

#### 4.2.2 Fit results

Fig 15 and Table 2 summarise the results of fitting the fake data with the input model (left) and a single ionization model (right). We fix the hydrogen column density in both of the fits, assuming this to be constrained in some other way. We see that the single ionization model under-predicts the source height with high statistical significance. This is consistent with [Svoboda et al. \(2012\)](#) and [Kammoun et al. \(2019\)](#), who found that using a single ionization zone can produce artificially steep power-law emissivity profiles (and lower source height corresponds to steeper emissivity: Fig 4). Previous spectral fitting studies using lamppost models assuming a single ionization parameter have therefore likely under-predicted the source height. The assumption of a single ionization parameter seems to have introduced a small bias in the spin measurement, although we find that the spin is under-predicted here, whereas many observational studies, particularly for AGN, yield near-maximal spin values. We also note that the disk inner radius is fixed to the ISCO in our fake data, but is often observed to reduce as the spectrum softens in the real data (e.g. [Plant et al. 2015](#); [García et al. 2015](#)). The large red wing of the iron line introduced by the ionization gradient appears to have been compensated by a larger value of  $\Gamma$  instead of a smaller value of  $r_{in}$ .

Interestingly, the single ionization fit includes a highly statistically significant ( $5.5\sigma$  from an F-test) low-ionization XILLVERCP component. Such a component is often required in fits to real spectra in order to account for enhanced distant reflection (e.g. from a flared outer disk, or from the

companion star). Our experiment here implies that the often uncomfortably high flux required for the distant reflector may, in part, be due to a modelling systematic introduced by assuming a single ionization parameter. The correct iron abundance is recovered for both fits, but we note that the best fitting single ionization model with no distant reflection component includes a super-solar iron abundance ( $A_{Fe} = 2.71^{+0.313}_{-0.229}$ ; errors are 90% confidence limits). This is interesting because super-solar iron abundances are now consistently measured in X-ray binaries, but it is not well understood why this should be the case ([García et al. 2018](#)). It is suspected that the iron abundance parameter is compensating for some missing physics in the models, such as higher electron density in the disk ( $n_e \sim 10^{20-22} \text{ cm}^{-3}$ ; [Tomsick et al. 2018](#)). The assumption of a single ionization parameter may also contribute to the high measured iron abundance in some cases.

## 5 EXAMPLE FITS FOR MRK 335

As a proof of principle, we apply the RELTRANS model to an archival *XMM-Newton* observation of the AGN Mrk 335 for which an iron K feature has previously been identified in the lag-energy spectrum ([Kara et al. 2013](#)). We choose this observation because it provides a good example of an iron K lag feature without the need for complications such as stacking multiple observations or dealing with photon pile-up (both of which are required for the Ark 564 lag-energy spectrum also featured in [Kara et al. 2013](#)). We find that, even though this frequency range displays clear signs of reverberation, a statistically acceptable fit to the real and imaginary parts of the cross-spectrum could only be achieved by including non-linear variability of the direct spectrum, which is beyond the scope of this paper but is introduced for the RELTRANS model in a companion paper ([Mastroserio et al. 2019](#)). We therefore instead fit only the time lags in a single frequency

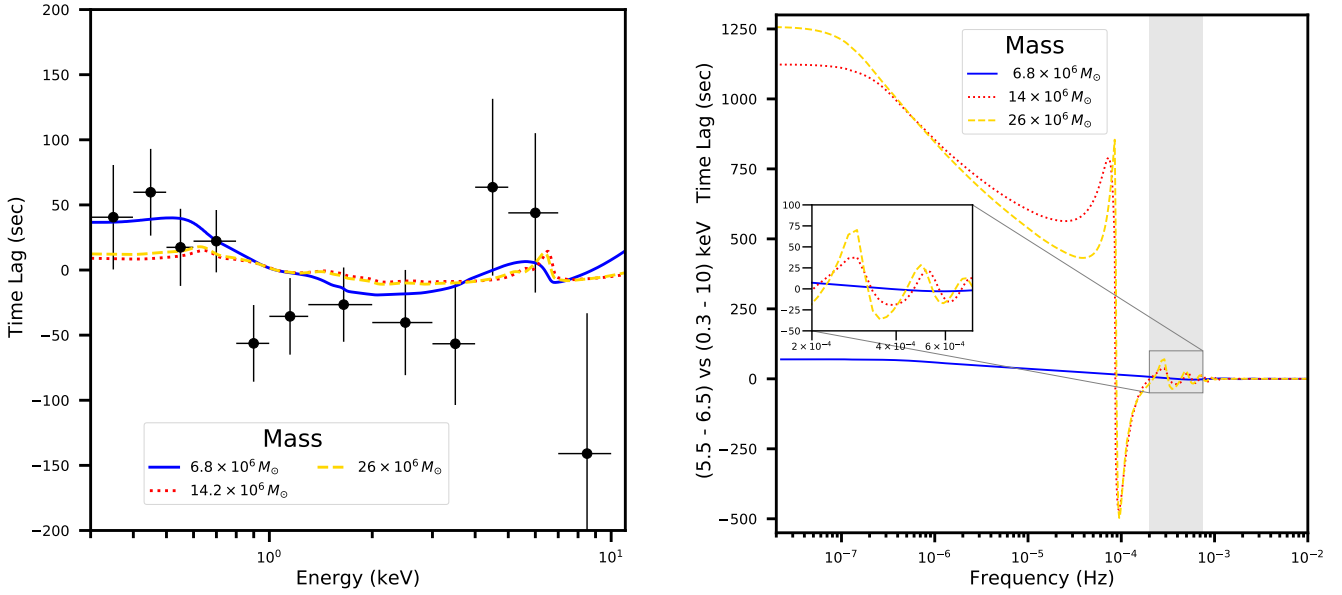


**Figure 16.** *Left:* Time lag as a function of energy in the frequency range  $[2-7.5] \times 10^{-4}$  Hz for *XMM-Newton* data from Mrk 335 (black points), alongside three RELTRANS model fits (reference band: 0.3–10 keV). For the blue solid line, the black hole mass is a free parameter, and for the red dotted and yellow dashed lines we fix it to two different optical reverberation values from the literature. *Right:* Time lag, averaged over the iron line region (5.5–6.5 keV), plotted against frequency for the same three models. We see that, in the frequency range used for the lag-energy spectrum (grey band), the models using the optical reverberation masses (red dotted and yellow dashed lines) are in the phase-wrapping regime whereas our best fitting model (blue solid line) is not.

range here, leaving a multi-frequency fit of real and imaginary parts of the cross-spectrum to a future paper.

### 5.1 Data

We consider the 133 ks *XMM-Newton* observation taken in 2006 (obs ID 0306870101) that was analysed by Kara et al. (2013). Following Kara et al. (2013), we consider only pn data, and reduce it using the *XMM-Newton* Science Analysis System (SAS v.11.0.0), applying the filters `PATTERN`  $\leq 4$  and `FLAG == 0`. We exclude background flares at the beginning and end of the observation (considering only times 252709714 to 252829414 seconds) and extract light curves with 10 second binning from 12 different energy bands, spaced roughly equally in the range 0.3–10 keV, from a circular region with 35 arcsec radius centred on the maximum of the source emission. We apply the SAS task `epiclccorr` for background subtractions and various corrections.

Again following Kara et al. (2013), we calculate the cross-spectrum between each of the 12 energy bands and a reference band that is the sum of all energy bands except for the current subject band (thereby ensuring statistical independence between the subject and reference bands; see e.g. Uttley et al. 2014). We average these 12 cross-spectra over the frequency range  $[2-7.5] \times 10^{-4}$  Hz, since this is the range for which ‘soft lags’ are observed (De Marco et al. 2013): i.e. fluctuations in the 0.3–0.8 keV band lag behind those in the 1–4 keV band (with the former assumed to be more reflection-dominated than the latter). We calculate energy dependent time lags by taking the argument of each frequency-averaged cross-spectrum and dividing by  $2\pi\nu$ , where  $\nu = 4.75 \times 10^{-4}$  Hz is the centre of the frequency range. We calculate error bars using the analytic

formula from Bendat & Piersol (2010, see also Nowak et al. 1999). Since the frequency resolution of the cross-spectra is  $d\nu = 8.35 \times 10^{-6}$  Hz, the  $[2-7.5] \times 10^{-4}$  Hz frequency range contains 65 frequency bins, meaning that the lag spectrum is Gaussian distributed and we can therefore fit models using the  $\chi^2$  statistic.

### 5.2 Fits to the lag-energy spectrum

Fig. 16 (left) shows the observed lag-energy spectrum of Mrk 335 (black points), which displays the iron K feature at  $\sim 6.4$  keV reported by Kara et al. (2013)<sup>5</sup>, alongside three RELTRANS model fits. A full treatment would employ a simultaneous fit to the time-averaged spectrum, which we will present in a future paper. For the purposes of this demonstration of the use of the model we instead fit only the lag spectrum, and avoid over-fitting by fixing most parameters to values constrained by a previous spectral analysis of these data (Keek & Ballantyne 2016). For the spin, disk inner radius, inclination angle, ionisation parameter, iron abundance, slope of the incident power-law and high energy cut-off, we use  $a = 0.89$ ,  $r_{\text{in}} = \text{ISCO}$ ,  $i = 30^\circ$ ,  $\log_{10} \xi = 2.68$ ,  $A_{\text{Fe}} = 3.9$ ,  $\Gamma = 1.95$  and  $(E_{\text{cut}})_{\text{obs}} = 300$  keV (we assume a constant ionisation parameter for simplicity). Following Kalberla et al. (2005), we fix  $N_h = 3.6 \times 10^{20} \text{ cm}^{-2}$ . We use the model configuration that outputs time lags accounting for line-of-sight absorption and the instrument response (`ReIm=6`), and calculates  $\phi_A$  self-consistently (`PHI_SET=1`). The remaining free parameters are black hole mass  $M$ , source

<sup>5</sup> Although note that we use a slightly different frequency range, and so our results are consistent but not identical.

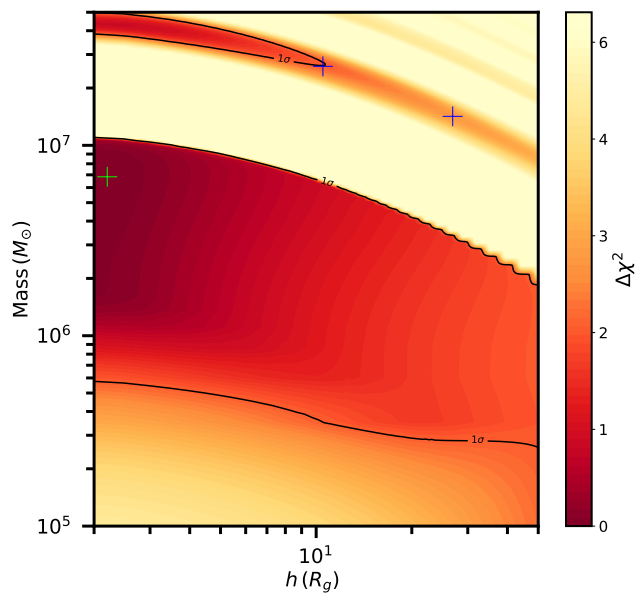


**Figure 17.** 2D  $\chi^2$  contour plot of black hole mass and source height resulting from fitting RELTRANS to the lag versus energy spectrum of Mrk 335 in the frequency range  $[2 - 7.5] \times 10^{-4}$  Hz. The green cross marks the best fit and the blue crosses mark the best fit for the two optical reverberation masses.

height  $h$  and the boost parameter  $1/\mathcal{B}$  (for which we set the hard ranges  $> 2 R_g$  and  $0 - 3$  respectively).

The blue solid line represents our best-fitting model, which has parameters  $M = 6.8^{+5.5}_{-5.9} \times 10^6 M_\odot$ ,  $h = 2.2^{+34}_{-p}$  and  $1/\mathcal{B} = 0.63^{+p}_{-0.48}$  ( $\chi^2/\text{d.o.f.} = 11.3/9$ ; errors are  $1\sigma$ ), where  $p$  indicates that a parameter is pegged at a hard limit. This value of mass is smaller than the optical reverberation measurements in the literature, with the two most recently published values being  $M = [14.2 \pm 3.7] \times 10^6 M_\odot$  (Peterson et al. 2004) and  $M = [26 \pm 8] \times 10^6 M_\odot$  (Grier et al. 2012). Chainakun et al. (2016) recently also fit an X-ray reverberation model to the same lag spectrum and obtained a best fitting mass of  $13.5 \times 10^6 M_\odot$ , albeit with poorly constrained errors due to the computational expense of their model. We investigate this apparent discrepancy by re-fitting our model with the mass fixed to the two optical reverberation values. The red dotted and yellow dashed lines in Fig. 16 (left) show the resulting best fits. The  $M = 14.2 \times 10^6 M_\odot$  fit has parameters  $h = 26.9$  and  $1/\mathcal{B} = 3$  ( $\chi^2/\text{d.o.f.} = 14.4/9$ ) and the  $M = 26 \times 10^6 M_\odot$  fit has parameters  $h = 10.5$  and  $1/\mathcal{B} = 3$  ( $\chi^2/\text{d.o.f.} = 13.7/9$ ). We see that these two high mass fits have very similar lag-energy spectra. We note that the iron line feature in our model (and in the model of Chainakun et al. 2016) is far less prominent than the Gaussian line feature in the empirical model plotted in Fig 8 of Kara et al. (2013). However our best fitting model, which has one less free parameter than their linear plus Gaussian model, provides a better statistical description of the data (the empirical model has  $\chi^2/\text{d.o.f.} = 13.22/8$ ).

An F-test reveals that our best-fitting mass is preferred to the Peterson et al. (2004), Grier et al. (2012) and Chainakun et al. (2016) mass values with only  $\lesssim 1.5 \sigma$  confidence. The reason why very different masses can give such

similar  $\chi^2$  values is particularly fascinating, and serves to illustrate the importance of fitting to multiple frequency ranges instead of just one. Fig. 16 (right) shows the lag averaged over the iron line energy range plotted against frequency for the three models (colours and line styles have the same meaning as in the left hand plot). The grey band denotes the frequency range used for our fits. We see that, averaged over this frequency range, the three models give roughly the same time lag as each other ( $\sim 10$  s). However, the two high mass models diverge enormously from our best fitting model at lower frequencies. We see that the high mass models are actually in the phase-wrapping regime in the frequency range used for the fit. This happens when the time lag between the direct and reflected signals is greater than  $\pi\nu$  or less than  $-\pi\nu$ , similar to the effect that leads to car wheels appearing to rotate backwards when viewed on film with a frame rate lower than the rotation frequency of the wheels. Note that the time lag between the two energy bands used for this figure is *not* greater than  $\pi\nu$  when phase wrapping starts. This is because of dilution: the time lag between *direct* and *reflected* components is  $> \pi\nu$ , but both energy bands contain some direct and some reflected X-rays (see the discussion in Uttley et al. 2014). Fig 17 is a 2D  $\chi^2$  contour plot of black hole mass and source height that illustrates this point further. We see there are two dark stripes corresponding to regions of statistically acceptable mass (plus several lighter stripes in the top right hand corner). The two optical reverberation masses fall in the upper stripe (blue crosses), which therefore corresponds to our phase-wrapped regime. Our best fit falls in the lower stripe (green cross), and the error estimate quoted above of  $\pm \sim 6 \times 10^6 M_\odot$  only considers this lower stripe. We also see an anti-correlation between mass and source height. This occurs because the light-crossing time lag depends on  $h \times R_g$ , and therefore an increase in  $h$  can be offset to some extent by a decrease in  $M$ .

At lower frequencies ( $\lesssim 10^{-5}$  Hz), the  $5.5 - 6.5$  keV reverberation lag for the high mass models is *far* larger than for the low mass model. This is partly due to the larger mass itself (i.e.  $1 R_g$  is a larger distance), and partly because the source height and boost parameter are both much larger in the high mass models (i.e. large  $h$  means the path-length difference is a greater number of gravitational radii, and large  $1/\mathcal{B}$  means that the reflection fraction is still high even though  $h$  is large, thus reducing dilution). This means that, in the frequency range used for the fits, the phase-wrapped time lag in the high mass models is roughly similar to the time lag in the low mass model. The high mass models therefore predict that there should be a negative iron K lag feature at  $\nu \sim 10^{-4}$  Hz and a very large positive lag at even lower frequencies, although these features will be heavily diluted by the intrinsic hard lags. Even though the lowest frequencies ( $\nu \lesssim 10^{-5}$  Hz) cannot be probed with currently available data, it should be possible to test these predictions in future by fitting a modified version of the model that additionally models hard lags as fluctuations in the photon index for a number of frequency ranges, yielding a robust mass measurement in the process. Of the models we explore here, the low mass model is the more plausible, due to the very high boost parameter (pegged to its hard upper limit) required for the high mass models, although the parameters will likely change once hard lags are accounted for in this

frequency range, which is necessary to also reproduce the observed variability amplitude. The results of [Chainakun et al. \(2016\)](#) instead favour a higher mass, and their model included an ionization profile and a simultaneous fit to the time-averaged spectrum. However, it is not clear whether or not their best fit was in the phase wrapping regime.

## 6 DISCUSSION

We have presented a public XSPEC reverberation mapping model that can be fit to the energy dependent complex cross-spectrum of black hole X-ray binaries and AGN for a range of Fourier frequencies. It is now common to fit the time-averaged spectrum with sophisticated relativistic reflection models. Our model is designed to be comparably user-friendly to the spectral models, but with the considerable extra functionality of also modelling the timing properties. This provides the opportunity for better geometrical constraints and entirely new black hole mass constraints.

### 6.1 Comparison with previous work

We have compared our model extensively to the existing spectral model `RELXILLP`, and find good agreement with the most recent version of that model. We did however find a very minor error in the [Bardeen et al. \(1972\)](#) expression for the Lorentz factor of a rotating disk element, which has propagated into the `RELXILLP` model and likely somewhat further into the literature (see Appendix A). However, we find the discrepancy is small enough to be inconsequential. Further bench marking against other spectral models (e.g. [Dovciak 2004](#); [Wilkins & Fabian 2012](#)) will be very useful.

Previous reverberation mapping modelling studies have mainly focused on AGN time lags ([Cackett et al. 2014](#); [Emmanoulopoulos et al. 2014](#); [Chainakun & Young 2015](#); [Caballero-Garcia et al. 2018](#)). Ours is the first public model to also consider variability amplitudes. Our model, similar to most previous studies, uses the lamppost geometry. There has been work to model more sophisticated geometries that self-consistently produce hard intrinsic lags through propagating mass accretion rate fluctuations ([Wilkins & Fabian 2013](#); [Wilkins et al. 2016](#)), but these models are too computationally expensive for fitting to data. The two blobs model of [Chainakun & Young \(2017\)](#), consisting of two lamppost sources, allows a slightly more realistic geometry that also can produce hard intrinsic lags but without prohibitive computational expense. Such a geometry can be used in our model, as long as the user fits for real and imaginary parts of the cross-spectrum rather than amplitude and time lags. In this case, two `RETRANS` model components with different source heights can simply be added together. Intrinsic lags are then produced if the amplitude and phase normalisations of the two components -  $\alpha_1(\nu)$ ,  $\alpha_2(\nu)$ ,  $\phi_{A1}(\nu)$  and  $\phi_{A2}(\nu)$  - are left as free parameters. This essentially models a lag between incident emission from the two lamppost sources, as in [Chainakun & Young \(2017\)](#).

### 6.2 Ionization profile

We include a self-consistently calculated radial disk ionization profile in our model and find that this has a signifi-

cant effect on the model outputs. There is some uncertainty over the radial disk density profile that should be used to calculate the ionization profile. Our model considers both a Shakura-Sunyaev zone A (radiation pressure dominated) density profile, and a constant density. Even assuming the [Shakura & Sunyaev \(1973\)](#) model to be exact, we still expect the density profile to depend on mass accretion rate, black hole mass and the viscosity parameter. In particular, the disks of X-ray binaries in faint hard states likely do not have a radiation pressure dominated zone, especially given the weight of evidence for disk truncation in this state (e.g. [Tomsick et al. 2009](#); [Ingram et al. 2017](#)). Interestingly though, this implies that there will be a point in the outburst at which the mass accretion rate has risen sufficiently for the inner disk to become radiation pressure dominated, leading to a change in ionization profile. Perhaps with careful modelling, this may be detectable with high quality data from current observatories such as *NICER* and *NuSTAR*, or future observatories such as *ATHENA*, *STROBE-X* or *Colibri* ([Ray et al. 2019](#); [Caiazzo et al. 2019](#)). Constraining this transition would provide useful insights into disk physics, such as estimating the viscosity parameter in the inner disk. Fitting the cross-spectrum for a wide range of frequencies in addition to the time-averaged spectrum will be far more constraining in this respect than only considering the spectrum.

Although we account for the ionization profile, we do not account for the dependence of the rest frame reflection spectrum on the density itself ([Garcia et al. 2016](#)). We use the public `XILLVER` and `XILLVERCP` grids, that are hardwired for  $n_e = 10^{15} \text{ cm}^{-3}$ . This value is more appropriate for the most massive AGN than for X-ray binaries, whose disks are expected to be much denser ( $n_e \propto 1/M$ , assuming the disk to be radiation pressure dominated and in vertical hydrostatic equilibrium). The main difference is a much higher disk temperature and therefore much more thermal radiation in soft X-rays. The effect of radially stratified density has not yet been explored.

When we generate fake data from a model with a self-consistent ionization profile and fit with a constant ionization model, we find that a narrow (non-relativistically smeared) reflection component is required in the fit with high statistical significance (although we note that a more systematic parameter exploration would be required to make strong conclusions). This is interesting because fits to real data commonly require such a narrow reflection component, which can be attributed to a distant reflector (e.g. [Garcia et al. 2015](#); [Ingram et al. 2017](#)). This can either take the form of a flared outer disk, the companion star for X-ray binaries, or the torus for AGN. However, the flux of the best-fitting narrow reflection component is often uncomfortably high. Our result suggests that these high fluxes could actually be down to a modelling systematic that could be at least in part alleviated by using an ionization profile. The timing-properties are also very sensitive to the ionization profile. Indeed [Chainakun et al. \(2016\)](#) found that the  $\sim 3 \text{ keV}$  dip present in the lag spectrum of a number of AGN could only be explained by stratification of the disk ionization parameter. We also note that, whereas a parameter combination can be found to allow a single ionization model to mimick the time-averaged spectrum produced by a model with self-

consistent ionization, additionally considering the time lags and variability amplitude should break the degeneracy.

We also found from our fits to fake data that a constant ionization model under-predicts the source height (consistent with the results of [Svoboda et al. 2012](#) and [Kammoun et al. 2019](#)). [Niedźwiecki et al. \(2016\)](#) noted two problems associated with the very low source heights measured by many spectral fitting studies of AGN and X-ray binaries (e.g. [Parker et al. 2014](#); [Kara et al. 2015](#); [Parker et al. 2015](#); [Degenaar et al. 2015](#); [Beuchert et al. 2017](#); [Wang et al. 2017](#)). First, the resulting suppression of the directly observed flux through gravitational redshift and lensing means that fits to bright sources such as Cygnus X-1 (e.g. [Parker et al. 2015](#); [Beuchert et al. 2017](#)) require an intrinsic source flux as high as  $\sim 50$  times the Eddington limit for a hard spectral state. Second, the intrinsic high energy cut-off implied by such a large source redshift is so high that runaway cooling should have long since been triggered by pair production (e.g. [Poutanen & Svensson 1996](#); [Fabian et al. 2012](#)). The higher source heights yielded by accounting for a realistic ionization profile alleviate both of these problems.

### 6.3 Time lags and instrument response

In Section 4.1, we show that failing to account for line-of-sight absorption and the instrument response matrix can significantly bias the predicted time lags. This bias is particularly prominent in the  $\lesssim 1$  keV energy range of *XMM-Newton* data, but has little to no effect in the  $\sim 2 - 10$  keV range. This may at least partly explain why studies of AGN that model the  $\sim 0.3 - 1$  vs  $\sim 1 - 10$  keV lags (e.g. [Emmanoulopoulos et al. 2014](#)) have returned lower source heights than those modeling the  $\sim 5 - 7$  vs  $\sim 2 - 4$  keV lags ([Epitropakis et al. 2016](#)). This is because ignoring the telescope response over-predicts the soft band lag for a given source height (see Fig 13), and so a very small source height is needed to still produce the fairly small lags present in the data. For frequency ranges in which the intrinsic hard lags are prominent, the response matrix bias can give rise to spurious features in the observed  $E \lesssim 1$  keV lag spectrum that look worryingly like the features in X-ray binary data previously attributed to thermal reverberation (e.g. [Uttley et al. 2011](#); [De Marco et al. 2017](#)). We conclude that the observation of GX 339-4 from [De Marco et al. \(2017\)](#) and [Mahmoud et al. \(2018\)](#) that we investigate does indeed contain a signature of thermal reverberation, but that the measured value of the lag may have been heavily biased by failure to account for the instrument response. [Mahmoud et al. \(2018\)](#) fit a transfer function model to the GX 339-4 data and measure a disk inner radius of  $\sim 20 R_g$ . However, their model only accounts for the effective area curve of *XMM-Newton* and not the redistribution matrix. Their inner radius value may therefore be an over-estimate, since the intrinsic lags are likely shorter than what is inferred from their analysis.

### 6.4 Black hole mass

Our proof-of-principle fit to the lag-energy spectrum of Mrk 335 in a single frequency range (Section 5) favours a black hole mass of  $\sim 7$  million  $M_\odot$  to the optical reverberation values in the literature of  $\sim 14$  million  $M_\odot$  ([Peterson et al. 2004](#))

and  $\sim 26$  million  $M_\odot$  ([Grier et al. 2012](#)), and the previous X-ray reverberation value of  $\sim 13.5$  million  $M_\odot$  ([Chainakun et al. 2016](#)), although the higher masses are only disfavoured with  $\lesssim 1.5\sigma$  confidence. The confidence range on the mass is very large for such a fit to a single frequency range, partly because the size of the reverberation lag is degenerate with the reflection fraction. However, our findings here demonstrate very effectively that this degeneracy will be eliminated by a simultaneous fit to multiple frequency ranges, since our best-fitting  $M = 6.8 \times 10^6 M_\odot$  model predicts a wildly different time lag signature at lower frequencies to the two higher mass models that we also explore. For this it will be vital to additionally model the intrinsic hard lags. In fact, we find that intrinsic hard lags are required in order to explain the variability amplitude in addition to the lags even in the frequency range explored here. This may therefore bias the black hole mass yielded by our current analysis. We will conduct a full multi-frequency analysis on the Mrk 335 data in a future paper, also simultaneously considering the variability amplitude and time-averaged spectrum (Mastroserio et al in prep). The resulting constraints on the black hole mass may enable some of the uncertainties associated with optical reverberation mapping to be addressed, most notably the uncertain geometry of the broad line region (typically parameterised by the constant  $f$ ). We note that the X-ray reverberation analysis of [Emmanoulopoulos et al. \(2014\)](#) returned a black hole mass estimate of  $M = 19.8^{+11.8}_{-10.5} \times 10^6 M_\odot$  for Mrk 335, which is again larger than our value. Their fit procedure was very different to ours and that of [Chainakun et al. \(2016\)](#). They fit for time lags between two broad energy bands as a function of frequency, and employed simplified assumptions regarding the energy dependence of reflected X-rays.

X-ray reverberation mapping can also be used to measure the mass of stellar-mass black holes in X-ray binary systems. In a companion paper, we constrain the mass of the black hole in Cygnus X-1 (Mastroserio et al submitted). We do however note that care must be taken to avoid frequency ranges dominated by quasi-periodic oscillations, given strong evidence that these are driven by geometric oscillations that are not modelled here ([Ingram & van der Klis 2015](#); [Ingram et al. 2016](#)).

### 6.5 Future modelling improvements

Our model is still very idealised, and there is much room for future improvement. We will in future extend our model to account for fluctuations in the power-law index of the illuminating spectrum (Mastroserio et al submitted). It will also be useful in future to include a non-zero disk scale height. [Taylor & Reynolds \(2018b\)](#) and [Taylor & Reynolds \(2018a\)](#) show that using the scale height expected for a radiation pressure dominated disk leads to steeper emissivity profiles, with spectral and timing properties consequently adjusted due to the signal being more dominated by the broader line and shorter time lags associated with the inner regions of the disk. Our calculation also assumes that the source is stationary, whereas emission would actually be boosted somewhat away from the disk if the source is actually a standing shock at the base of the outflowing jet, as is often suggested ([Markoff et al. 2005](#); [Dauser et al. 2013](#)). We do however include a ‘boosting parameter’ that approximates

this affect by reducing the reflection fraction. If the user takes the lamppost geometry seriously and finds that the boosting parameter is statistically required in the fit to be less than unity, they can conclude that the source is moving away from the disk. Niedźwiecki & Zdziarski (2018) recently pointed out that in a lamppost geometry, we should also sometimes see the other lamppost source on the underside of the disk and we should also see photons from the top lamppost whose trajectories have bent around the black hole and into our line of sight - particularly if the disk is truncated. We do not include these effects, which will presumably be blocked or significantly altered by material inside of the disk.

We use the models `XILLVER` and `XILLVERCP` to compute the rest frame reflection spectrum (García & Kallman 2010; García et al. 2013), which are state-of-the-art, but still include approximations that can be addressed in future. A constant vertical density profile is assumed, which returns a very different  $E \lesssim 1$  keV reflection spectrum from a calculation assuming vertical hydrostatic equilibrium (Nayakshin et al. 2000; Done & Nayakshin 2007; Różańska et al. 2011; Vincent et al. 2016). We note, however, that recent numerical simulations indicate that the vertical density profile of a magnetic pressure dominated disk is roughly constant near the surface (Jiang et al. 2019). The largest approximation of all is likely the lamppost model itself, and so it will be important to explore more realistic geometries in future (Zhang et al. 2019).

## 7 CONCLUSIONS

The X-ray reverberation models `RELTRANS` and `RELTRANS-CP` are now publicly available for use in `XSPEC`. The source code and usage instructions can be downloaded from <https://adingram.bitbucket.io/>. The models can be used to simultaneously fit the real and imaginary parts of the energy-dependent cross-spectrum for a wide range of Fourier frequencies, plus the time-averaged spectrum. Intrinsic hard lags can be accounted for by using two model components added together. The model is designed to be user friendly for the beginner but flexible for the advanced user, with environment variables specifying model properties and advanced options. We find that modelling systematics have likely led to artificially low source heights being measured in the literature. We also find that bright distant reflection component often statistically required in spectral fits can at least partially be explained by the radial profile of the disk ionization parameter. Our proof-of-principle fits to the lag-energy spectrum of the Seyfert galaxy Mrk 335 return a smaller mass for the central black hole than previous optical reverberation mapping analyses ( $\sim 7$  million compared with  $\sim 14 - 26$  million  $M_\odot$ ), which we will investigate in more detail in future.

## ACKNOWLEDGEMENTS

A. I. acknowledges support from the Royal Society and valuable discussions with Chris Reynolds and George Ellis. G.M. acknowledges support from NWO.

## REFERENCES

Arévalo P., Uttley P., 2006, *MNRAS*, **367**, 801  
 Bardeen J. M., Press W. H., Teukolsky S. A., 1972, *ApJ*, **178**, 347  
 Basak R., Zdziarski A. A., Parker M., Islam N., 2017, *MNRAS*, **472**, 4220  
 Benda J. S., Piersol A. G., 2010, Random Data: Analysis and measurement procedures; 4th edition. Wiley, 2010  
 Beuchert T., et al., 2017, *A&A*, **603**, A50  
 Caballero-Garcia M. D., Papadakis I. E., Dovciak M., Bursa M., Epitropakis A., Karas V., Svoboda J., 2018, preprint, ([arXiv:1804.03503](https://arxiv.org/abs/1804.03503))  
 Cackett E. M., Zoghbi A., Reynolds C., Fabian A. C., Kara E., Uttley P., Wilkins D. R., 2014, *MNRAS*, **438**, 2980  
 Caiazzo I., et al., 2019, arXiv e-prints, *Campaña S., Stella L.*, 1995, *MNRAS*, **272**, 585  
 Carter B., 1968, *Phys. Rev.*, **174**, 1559  
 Chainakun P., Young A. J., 2015, *MNRAS*, **452**, 333  
 Chainakun P., Young A. J., 2017, *MNRAS*, **465**, 3965  
 Chainakun P., Young A. J., Kara E., 2016, *MNRAS*, **460**, 3076  
 Dauser T., García J., Wilms J., Böck M., Brenneman L. W., Falanga M., Fukumura K., Reynolds C. S., 2013, *MNRAS*, **430**, 1694  
 Dauser T., García J., Parker M. L., Fabian A. C., Wilms J., 2014, *MNRAS*, **444**, L100  
 Dauser T., García J., Walton D. J., Eikmann W., Kallman T., McClintock J., Wilms J., 2016, *A&A*, **590**, A76  
 De Marco B., Ponti G., Cappi M., Dadina M., Uttley P., Cackett E. M., Fabian A. C., Miniutti G., 2013, *MNRAS*, **431**, 2441  
 De Marco B., Ponti G., Muñoz-Darias T., Nandra K., 2015, *ApJ*, **814**, 50  
 De Marco B., et al., 2017, *MNRAS*, **471**, 1475  
 Degenaar N., Miller J. M., Chakrabarty D., Harrison F. A., Kara E., Fabian A. C., 2015, *MNRAS*, **451**, L85  
 Dexter J., Agol E., 2009, *ApJ*, **696**, 1616  
 Done C., Diaz Trigo M., 2010, *MNRAS*, **407**, 2287  
 Done C., Nayakshin S., 2007, *MNRAS*, **377**, L59  
 Done C., Gierlinski M., Kubota A., 2007, *A&A*, **461**, 581  
 Dovciak M., 2004, PhD thesis  
 Eardley D. M., Lightman A. P., Shapiro S. L., 1975, *ApJ*, **199**, L153  
 Ellis G. F. R., 2007, *General Relativity and Gravitation*, **39**, 1047  
 Ellis G. F. R., 2009, *General Relativity and Gravitation*, **41**, 581  
 Emmanoulopoulos D., Papadakis I. E., Dovčiak M., McHardy I. M., 2014, *MNRAS*, **439**, 3931  
 Epitropakis A., Papadakis I. E., 2017, *MNRAS*, **468**, 3568  
 Epitropakis A., Papadakis I. E., Dovčiak M., Pecháček T., Emmanoulopoulos D., Karas V., McHardy I. M., 2016, *A&A*, **594**, A71  
 Etherington I. M. H., 1933, *Philosophical Magazine*, **15**  
 Fabian A. C., Rees M. J., Stella L., White N. E., 1989, *MNRAS*, **238**, 729  
 Fabian A. C., et al., 2009, *Nature*, **459**, 540  
 Fabian A. C., et al., 2012, *MNRAS*, **424**, 217  
 Fender R., et al., 1999, *ApJ*, **519**, L165  
 Galeev A. A., Rosner R., Vaiana G. S., 1979, *ApJ*, **229**, 318  
 García J., Kallman T. R., 2010, *ApJ*, **718**, 695  
 García J., Dauser T., Reynolds C. S., Kallman T. R., McClintock J. E., Wilms J., Eikmann W., 2013, *ApJ*, **768**, 146  
 García J., et al., 2014, *ApJ*, **782**, 76  
 García J. A., Steiner J. F., McClintock J. E., Remillard R. A., Grinberg V., Dauser T., 2015, *ApJ*, **813**, 84  
 García J. A., Fabian A. C., Kallman T. R., Dauser T., Parker M. L., McClintock J. E., Steiner J. F., Wilms J., 2016, *MNRAS*, **462**, 751  
 García J. A., Kallman T. R., Bautista M., Mendoza C., Deprince J., Palmeri P., Quinet P., 2018, preprint, ([arXiv:1805.00581](https://arxiv.org/abs/1805.00581))  
 Gendreau K. C., et al., 2016, in Space Telescopes and In-

strumentation 2016: Ultraviolet to Gamma Ray. p. 99051H, [doi:10.1117/12.2231304](https://doi.org/10.1117/12.2231304)

George I. M., Fabian A. C., 1991, *MNRAS*, **249**, 352

Gilfanov M., Churazov E., Revnivtsev M., 2000, *MNRAS*, **316**, 923

Grier C. J., et al., 2012, *ApJ*, **744**, L4

Haardt F., Maraschi L., 1991, *ApJ*, **380**, L51

Harrison F. A. e. a., 2013, *ApJ*, **770**, 103

Heida M., Jonker P. G., Torres M. A. P., Chiavassa A., 2017, *ApJ*, **846**, 132

Ichimaru S., 1977, *ApJ*, **214**, 840

Ingram A., van der Klis M. v. d., 2013, *MNRAS*, **434**, 1476

Ingram A., van der Klis M., 2015, *MNRAS*, **446**, 3516

Ingram A., Maccarone T. J., Poutanen J., Krawczynski H., 2015, *ApJ*, **807**, 53

Ingram A., van der Klis M., Middleton M., Done C., Altamirano D., Heil L., Uttley P., Axelsson M., 2016, *MNRAS*, **461**, 1967

Ingram A., van der Klis M., Middleton M., Altamirano D., Uttley P., 2017, *MNRAS*, **464**, 2979

Jansen F., et al., 2001, *A&A*, **365**, L1

Jiang Y.-F., Blaes O., Stone J., Davis S. W., 2019, arXiv e-prints,

Kalberla P. M. W., Burton W. B., Hartmann D., Arnal E. M., Bajaja E., Morras R., Pöppel W. G. L., 2005, *A&A*, **440**, 775

Kammoun E. S., Domček V., Svoboda J., Dovčiak M., Matt G., 2019, *MNRAS*, **485**, 239

Kara E., Fabian A. C., Cackett E. M., Uttley P., Wilkins D. R., Zoghbi A., 2013, *MNRAS*, **434**, 1129

Kara E., et al., 2015, *MNRAS*, **449**, 234

Kara E., Alston W. N., Fabian A. C., Cackett E. M., Uttley P., Reynolds C. S., Zoghbi A., 2016, *MNRAS*, **462**, 511

Kara E., et al., 2019, *Nature*, **565**, 198

Keek L., Ballantyne D. R., 2016, *MNRAS*, **456**, 2722

Kolehmainen M., Done C., Díaz Trigo M., 2014, *MNRAS*, **437**, 316

Kotov O., Churazov E., Gilfanov M., 2001, *MNRAS*, **327**, 799

Laor A., 1991, *ApJ*, **376**, 90

Lightman A. P., Rybicki G. B., 1980, *ApJ*, **236**, 928

Lindquist R. W., 1966, *Annals of Physics*, **37**, 487

Mahmoud R. D., Done C., 2018, preprint, ([arXiv:1803.04811](https://arxiv.org/abs/1803.04811))

Mahmoud R. D., Done C., De Marco B., 2018, preprint, ([arXiv:1811.06911](https://arxiv.org/abs/1811.06911))

Markoff S., Nowak M. A., Wilms J., 2005, *ApJ*, **635**, 1203

Martocchia A., Matt G., 1996, *MNRAS*, **282**, L53

Mastroserio G., Ingram A., van der Klis M., 2018, *MNRAS*, **475**, 4027

Matt G., Perola G. C., Piro L., 1991, *A&A*, **247**, 25

McHardy I. M., Papadakis I. E., Uttley P., Page M. J., Mason K. O., 2004, *MNRAS*, **348**, 783

Middleton M., 2016, in Bambi C., ed., *Astrophysics and Space Science Library* Vol. 440, *Astrophysics of Black Holes: From Fundamental Aspects to Latest Developments*. p. 99 ([arXiv:1507.06153](https://arxiv.org/abs/1507.06153)), [doi:10.1007/978-3-662-52859-4\\_3](https://doi.org/10.1007/978-3-662-52859-4_3)

Miller J. M., 2007, *ARA&A*, **45**, 441

Miller L., Turner T. J., Reeves J. N., 2008, *A&A*, **483**, 437

Miller J. M., et al., 2013, *ApJ*, **775**, L45

Misner C. W., Thorne K. S., Wheeler J. A., 1973, *Gravitation*. San Francisco: W.H. Freeman and Co., 1973

Miyamoto S., Kitamoto S., 1991, *ApJ*, **374**, 741

Miyamoto S., Kitamoto S., Mitsuda K., Dotani T., 1988, *Nature*, **336**, 450

Mushtukov A. A., Ingram A., van der Klis M., 2018, *MNRAS*, **474**, 2259

Nayakshin S., Kazanas D., Kallman T. R., 2000, *ApJ*, **537**, 833

Niedźwiecki A., Zdziarski A. A., 2018, *MNRAS*,

Niedźwiecki A., Zdziarski A. A., Szanecki M., 2016, *ApJ*, **821**, L1

Novikov I. D., Thorne K. S., 1973, in Dewitt C., Dewitt B. S., eds, *Black Holes (Les Astres Occlus)*. Gordon and Breach, New York, pp 343–450

Nowak M. A., Vaughan B. A., Wilms J., Dove J. B., Begelman M. C., 1999, *ApJ*, **510**, 874

Papadakis I. E., Nandra K., Kazanas D., 2001, *ApJ*, **554**, L133

Parker M. L., et al., 2014, *MNRAS*, **443**, 1723

Parker M. L., et al., 2015, preprint, ([arXiv:1506.00007](https://arxiv.org/abs/1506.00007))

Patrick A. R., Reeves J. N., Porquet D., Markowitz A. G., Braito V., Lobban A. P., 2012, *MNRAS*, **426**, 2522

Peterson B. M., et al., 2004, *ApJ*, **613**, 682

Plant D. S., Fender R. P., Ponti G., Muñoz-Darias T., Coriat M., 2014, *MNRAS*, **442**, 1767

Plant D. S., Fender R. P., Ponti G., Muñoz-Darias T., Coriat M., 2015, *A&A*, **573**, A120

Poutanen J., Svensson R., 1996, *ApJ*, **470**, 249

Rapisarda S., Ingram A., Kalamkar M., van der Klis M., 2016, *MNRAS*, **462**, 4078

Rapisarda S., Ingram A., van der Klis M., 2017a, *MNRAS*, **469**, 2011

Rapisarda S., Ingram A., van der Klis M., 2017b, *MNRAS*, **472**, 3821

Ray P. S., et al., 2019, arXiv e-prints,

Reis R. C., Fabian A. C., Ross R. R., Miller J. M., 2009, *MNRAS*, **395**, 1257

Reynolds C. S., 2019, *Nature Astronomy*, **3**, 41

Reynolds C. S., Nowak M. A., 2003, *Phys. Rep.*, **377**, 389

Reynolds C. S., Young A. J., Begelman M. C., Fabian A. C., 1999, *ApJ*, **514**, 164

Risaliti G., et al., 2013, *Nature*, **494**, 449

Ross R. R., Fabian A. C., 1993, *MNRAS*, **261**, 74

Róžańska A., Madej J., Konorski P., Sałowski A., 2011, *A&A*, **527**, A47

Shakura N. I., Sunyaev R. A., 1973, *A&A*, **24**, 337

Stella L., 1990, *Nature*, **344**, 747

Sunyaev R. A., Truemper J., 1979, *Nature*, **279**, 506

Svoboda J., Dovčiak M., Goosmann R. W., Jethwa P., Karas V., Miniutti G., Guainazzi M., 2012, *A&A*, **545**, A106

Tanaka Y., et al., 1995, *Nature*, **375**, 659

Taylor C., Reynolds C. S., 2018a, preprint, ([arXiv:1808.07877](https://arxiv.org/abs/1808.07877))

Taylor C., Reynolds C. S., 2018b, *ApJ*, **855**, 120

Thorne K. S., Price R. H., 1975, *ApJ*, **195**, L101

Tomsick J. A., Yamaoka K., Corbel S., Kaaret P., Kalemci E., Migliari S., 2009, *ApJ*, **707**, L87

Tomsick J. A., et al., 2018, *ApJ*, **855**, 3

Uttley P., Wilkinson T., Cassatella P., Wilms J., Pottschmidt K., Hanke M., Böck M., 2011, *MNRAS*, **414**, L60

Uttley P., Cackett E. M., Fabian A. C., Kara E., Wilkins D. R., 2014, *A&ARv*, **22**, 72

Vincent F. H., Róžańska A., Zdziarski A. A., Madej J., 2016, *A&A*, **590**, A132

Walton D. J., Nardini E., Fabian A. C., Gallo L. C., Reis R. C., 2013, *MNRAS*, **428**, 2901

Wang Y., Méndez M., Sanna A., Altamirano D., Belloni T. M., 2017, *MNRAS*, **468**, 2256

Wilkins D. R., Fabian A. C., 2012, *MNRAS*, **424**, 1284

Wilkins D. R., Fabian A. C., 2013, *MNRAS*, **430**, 247

Wilkins D. R., Cackett E. M., Fabian A. C., Reynolds C. S., 2016, *MNRAS*, **458**, 200

Wilms J., Allen A., McCray R., 2000, *ApJ*, **542**, 914

Xu Y., et al., 2018, *ApJ*, **852**, L34

Yang X., Wang J., 2013, *ApJS*, **207**, 6

Zdziarski A. A., Johnson W. N., Magdziarz P., 1996, *MNRAS*, **283**, 193

Zhang W., Dovčiak M., Bursa M., 2019, arXiv e-prints,

Zoghbi A., Fabian A. C., Reynolds C. S., Cackett E. M., 2012, *MNRAS*, **422**, 129

Życki P. T., Done C., Smith D. A., 1999, *MNRAS*, **309**, 561

van der Klis M., Hasinger G., Stella L., Langmeier A., van Paradijs J., Lewin W. H. G., 1987, *ApJ*, **319**, L13

## APPENDIX A: AREA OF A DISK RING

The proper area of a disk annulus of width  $dr$  as measured by a stationary observer is given by  $d^2x = 2\pi\sqrt{g_{rr}g_{\phi\phi}}dr$  (see e.g. Wilkins & Fabian 2012). The disk area element we are after for our calculation is measured in the disk frame, bringing in a factor of  $\gamma^\phi$ , which is the Lorentz factor of the orbiting disk element. Substituting in the components of the Kerr metric gives

$$\frac{dA_{\text{ring}}}{dr} = 2\pi\gamma^\phi\sqrt{\frac{r^4 + a^2r^2 + 2a^2r}{r^2 - 2r + a^2}}. \quad (\text{A1})$$

This equation agrees with the formula derived by Wilkins & Fabian (2012) and Dauser et al. (2013), except for a small typographical error in Dauser et al. (2013). We see that, in the limit  $r \gg 2$ , this reduces to  $2\pi r$ , as we would expect.

Formulae for the Lorentz factor are presented in Bardeen et al. (1972) (hereafter BPT72) and Dauser et al. (2013). However, a very small error in BPT72 has propagated into the later literature. We therefore present a derivation here. In order to do this, we must first define a local non-rotating frame (LNRF) in which  $r = \text{constant}$ ,  $\theta = \text{constant}$  and  $\phi = \omega t + \text{constant}$ . Here,  $\omega = -g_{t\phi}/g_{\phi\phi}$  is the term that allows the reference frame to rotate with inertial frames (i.e. the frame dragging effect). For any stationary, axisymmetric, asymptotically flat spacetime, we can write the line element  $ds^2 = g_{\mu\nu}dx^\mu dx^\nu$  as

$$ds^2 = -e^{2\nu}dt^2 + e^{2\psi}(d\phi - \omega dt)^2 + e^{2\mu_1}dr^2 + e^{2\mu_2}d\theta^2, \quad (\text{A2})$$

where the exponentials are defined in equations 2.3 and 2.5 of BPT72 for the case of the Kerr metric. Setting  $M = 1$  in the BPT72 equations gives the dimensionless units we employ here.

We can represent the 4-velocity in the LNRF as  $u^{(a)} = u^\mu e_\mu^{(a)}$ , where the components of the tetrad of basis vectors are given by  $e^{(i)} = e_\mu^{(i)}dx^\mu$ . The (covariant) tetrad of basis vectors for the LNRF is (BPT72 equation 3.2)

$$e^{(t)} = e^\nu dt, \quad e^{(r)} = e^{\mu_1}dr, \quad e^{(\theta)} = e^{\mu_2}d\theta, \quad e^{(\phi)} = -\omega e^\psi dt + e^\psi d\phi, \quad (\text{A3})$$

where it is a long-standing travesty that the letter  $e$  is used both for the basis vectors and as the exponential number (we try to clear this up by using an italicised font for the basis vectors). This gives

$$e^{(t)}_\mu = (e^\nu, 0, 0, 0), \quad e^{(r)}_\mu = (0, e^{\mu_1}, 0, 0), \quad e^{(\theta)}_\mu = (0, 0, e^{\mu_2}, 0), \quad e^{(\phi)}_\mu = (-\omega e^\psi, 0, 0, e^\psi). \quad (\text{A4})$$

The covariant tetrad can be derived from the definition  $e_\mu^{(a)}e_\nu^{(b)}g^{\mu\nu} = \eta^{(a)(b)}$ , and the contravariant tetrad from  $e_{(a)}^\mu e_{(b)}^\nu g_{\mu\nu} = \eta_{(a)(b)}$ , where  $\eta$  is the Minkowski metric.

The 3-velocity is  $v^{(i)} = u^{(i)}/u^t$ . For circular, equatorial orbits, the only non-zero component of the 3-velocity is the  $\phi$  component, which is given by

$$v^{(\phi)} = (\Omega_\phi - \omega)e^{\psi-\nu} \quad (\text{A5})$$

where  $\Omega_\phi = u^\phi/u^t$  is the angular velocity of the disk element. In the Kerr metric, this is  $\Omega_\phi = \pm 1/(r^{3/2} \pm a)$ , where the top and bottom signs are respectively for prograde and retrograde spin. Equation (A5) is the same as equation 3.10 in BPT72 except for a small typographical error in the index of the exponential in the BPT72 version. Subbing in the Kerr metric gives

$$v^{(\phi)} = \frac{r^2 + a^2 - 2ar^{1/2} + 2r^{-1}(a^2 \pm a^2)}{\Delta^{1/2}(r^{3/2} \pm a)}, \quad (\text{A6})$$

where  $\Delta = r^2 - 2r + a^2$ . The Lorentz factor is then simply given by  $\gamma^\phi = [1 - (v^{(\phi)})^2]^{-1/2}$ . Equation (A6) agrees with equation 3.11a in BPT72 for prograde spin but not for retrograde. Equation 10 in Dauser et al. (2013) can be reproduced by taking equation 3.11a from BPT72 and dropping the  $\pm$  and  $\mp$  signs. Therefore, our equation (A6) is valid for prograde and retrograde spins, whereas the equivalent equations from BPT72 and Dauser et al. (2013) (and potentially many other references) are only strictly accurate for prograde spin. In practice, the inaccuracy introduced by these mistakes is very small and need not be worried about.

## APPENDIX B: BLUESHIFT FACTORS AND ANGLES

Here we present the formulae used to calculate the various blueshift factors and angles. The covariant form of the tangent 4-vector of photons following geodesics in the Kerr metric is (see e.g. Bardeen et al. 1972; Dauser et al. 2013)

$$(\mathbf{k})_\mu = (-1, \pm\sqrt{V_r}/\Delta, \pm|q|, 0), \quad (\text{B1})$$

where  $q$  is Carter's constant (Carter 1968) and

$$\Delta = r^2 - 2r + a^2; \quad V_r = (r^2 + a^2)^2 - \Delta(q^2 + a^2). \quad (\text{B2})$$

Carter's constant for 'incident' photons propagating from source to disk is (e.g. Dovciak 2004)

$$q_i^2 = \frac{\sin\delta(h^2 + a^2)^2}{h^2 - 2h + a^2} - a^2, \quad (\text{B3})$$

and Carter's constant for 'emergent' photons propagating from a disk element to the observer is (e.g. Dovciak 2004; Ingram et al. 2015)

$$q_e^2 = \beta^2 + \cos^2 i (\alpha^2 - a^2). \quad (\text{B4})$$

4-velocity can be expressed as

$$\mathbf{u}^\mu = \frac{\Omega^\mu}{\sqrt{-g_{\alpha\beta}\Omega^\alpha\Omega^\beta}}, \quad \text{where} \quad \Omega^\mu \equiv \frac{d\mathbf{x}^\mu}{dt}. \quad (\text{B5})$$

The 4-velocity of the disk element is therefore

$$(\mathbf{u}_d)^\mu = u_d^t(1, 0, 0, \Omega_\phi); \quad \Omega_\phi = \frac{\pm 1}{r^{3/2} \pm a}; \quad u_d^t = \left\{ 1 - \frac{2}{r} + \frac{4a\Omega_\phi}{r} - \left[ r^2 + a^2 \left( 1 + \frac{2}{r} \right) \right] \Omega_\phi^2 \right\}^{-1/2}, \quad (\text{B6})$$

and the 4-velocity of the stationary source is

$$(\mathbf{u}_s)^\mu = \frac{1}{\sqrt{-g_{tt}}}(1, 0, 0, 0) = \sqrt{\frac{h^2 + a^2}{h^2 - 2h + a^2}}(1, 0, 0, 0). \quad (\text{B7})$$

The blueshift seen by an observer on the disk patch is therefore

$$g_{sd}(r) = \frac{(k_i)_\mu(u_d)^\mu}{(k_i)_\nu(u_s)^\nu} = \frac{(u_d)^t}{(u_s)^t} = \sqrt{\frac{h^2 - 2h + a^2}{h^2 + a^2}} \left\{ 1 - \frac{2}{r} + \frac{4a\Omega_\phi}{r} - \left[ r^2 + a^2 \left( 1 + \frac{2}{r} \right) \right] \Omega_\phi^2 \right\}^{-1/2}. \quad (\text{B8})$$

It follows that the blueshift experienced by photons propagating from the stationary lamppost source to a distant stationary observer is

$$g_{so} = \frac{1}{u_s^t} = \sqrt{\frac{h^2 - 2h + a^2}{h^2 + a^2}}. \quad (\text{B9})$$

The cosine of the incidence angle is given by

$$\mu_i = -\frac{(k_i)_\mu e_{(\theta)}^\mu}{(k_i)_\nu(u_d)^\nu} = \frac{(k_i)_\theta e_{(\theta)}^\theta}{(u_d)^t} = \frac{(q_i/r)}{(u_d)^t}, \quad (\text{B10})$$

because the  $\theta$  component of the contravariant tetrad of basis vectors is  $e_{(\theta)}^\theta = 1/r$ . For the blueshift experienced by emergent photons propagating from disk element to observer,  $g_{do}(r, \phi)$ , we use equation (4) from Ingram et al. (2017). This is accurate for a razor thin disk in the black hole equatorial plane. The cosine of the emission angle is

$$\mu_e = \frac{(k_e)_\mu e_{(\theta)}^\mu}{(k_e)_\nu(u_d)^\nu} = g_{do}(r, \phi)(k_e)_\theta e_{(\theta)}^\theta = g_{do}(r, \phi) \frac{q_e}{r}. \quad (\text{B11})$$

## APPENDIX C: ENVIRONMENT VARIABLES

The environment variables used by the model as listed in Table C1. All have sensible default values that the user can override, for example to change the model resolution or explore different radial ionization profiles.

This paper has been typeset from a  $\text{TeX}/\text{L}\text{AT}\text{E}\text{X}$  file prepared by the author.

| Name               | Function  | Possible values | Default value |
|--------------------|---|-----------------|---------------|
| REV_VERB           | Sets the verbose level.   | 0-1             | 0             |
| PHI_SET            | Sets whether $\phi_A$ is calculated self-consistently (1) using equation 25 or set by the model parameter <code>phiA</code> (0).  | 0-1             | 0             |
| RMF_SET            | Name (including path) of the instrument response file. If the code is in a mode requiring an instrument response, the user is prompted for this.  | string          | none          |
| ARF_SET            | Name (including path) of the instrument ancillary response file. This is not required if a .rsp file is entered.  | string          | none          |
| MU_ZONES           | Sets how many bins of $\mu_e(r, \phi)$ are used for the calculation. If this is set to 1, $\mu_e = \cos i$ is assumed.  | 1-10            | 5             |
| ECUT_ZONES         | Sets how many bins of $g_{sd}(r)$ are used for the calculation. If this is set to 1, it is assumed that the high energy cut-off seen by each disk ring is equal to $E_{cut}$ rather than $g_{sd}(r)E_{cut}$ .   | 1-10            | 5             |
| ION_ZONES          | Sets how many bins of $\log_{10} \xi(r)$ are used for the calculation. If this is set to 1, the ionization is assumed to be constant and determined by the input model parameter <code>logxi</code> . Otherwise, a radial ionization profile is used, with <code>logxi</code> setting the normalisation of the profile. | 1-100           | 10            |
| A_DENSITY          | Sets whether the radial ionization profile is calculated assuming a constant disk density (0), or assuming a zone A Shakura-Sunyaev disk density profile (1). The parameter <code>logxi</code> respectively sets exactly or roughly the peak value of $\log_{10} \xi(r)$ for the former and latter cases.               | 0-1             | 1             |
| GRID               | Name of geodesics grid (with full path). If a value is given, the grid is used to calculate an interpolated transfer function. Otherwise, all geodesics are calculated on the fly. Use of the grid is faster if $a$ and $i$ are free parameters, and the on the fly calculation is faster if they are fixed.            | string          | null          |
| RELXILL_TABLE_PATH | RELXILL variable: points to the directory containing the XILLVER tables.  | string          | null          |

**Table C1.** Environment variables. The default variables are used if the user does not set any of the above variables.